ATLAS CONF Note

ATLAS-CONF-2021-008

March 23, 2021

Search for new phenomena in pp collisions in final states with tau leptons, b-jets, and missing transverse momentum with the ATLAS detector

The ATLAS Collaboration

A search for new phenomena in final states with hadronically decaying tau leptons, b-jets, and missing transverse momentum is presented. The analyzed dataset comprises pp collision data at a center-of-mass energy of $\sqrt{s}$ = 13 TeV with an integrated luminosity of 139 fb^{-1}, delivered by the Large Hadron Collider and recorded with the ATLAS detector from 2015 to 2018. The observed data are compatible with the expected Standard Model background. The results are interpreted in simplified models for two different scenarios. The first model considers pair production of supersymmetric top squarks, each of which decays into a b-quark, a neutrino and a supersymmetric tau slepton. Each tau slepton in turn decays into a tau lepton and a nearly massless supersymmetric gravitino. Within this model, top-squark masses of 1.4 TeV can be excluded at the 95 % confidence level over a wide range of tau-slepton masses. The second model considers pair production of scalar leptoquarks with decays into third-generation leptons and quarks. Depending on the branching fraction into charged leptons, leptoquarks with masses up to around 1.25 TeV can be excluded at the 95 % confidence level. In addition, model-independent upper limits are set on the cross section of processes beyond the Standard Model.

ATLAS-CONF-2021-008
27 March 2021

© 2021 CERN for the benefit of the ATLAS Collaboration.
Reproduction of this article or parts of it is allowed as specified in the CC-BY-4.0 license.

1 Introduction

The Standard Model (SM) of particle physics has been verified to high precision. Despite its success, several observations have been made which have exposed the theory's shortcomings in various aspects and fostered new theoretical ideas. Supersymmetry (SUSY) [1–7] is a framework for models that extend the symmetries underlying the SM by introducing superpartners of the known bosons and fermions with the same quantum numbers but a spin difference of half a unit. These models can address the gauge hierarchy problem [8–11]. When conservation of R-parity [12] is assumed, the lightest supersymmetric particle is stable and may provide a candidate particle for the cold dark matter component of the universe [13, 14]. The introduction of supersymmetric partner particles can also modify the renormalisation group equations in such a way that the coupling constants of the SM electromagnetic, weak and strong interaction meet in one point at some high energy scale as expected in a grand unified theory [15]. Another possibility to extend the SM is to embed the SM symmetry group in an overarching symmetry group, such as SU(5) [16] in grand unification, which gives rise to a new class of bosons that carry non-zero baryon and lepton quantum numbers and are charged under all SM gauge groups. These hypothetical leptoquarks (LQ) appear in a variety of SM extensions [17–21] and would provide an explanation for the structural similarities of the quark and lepton sectors in the SM. Processes mediated by the exchange of LQs can violate lepton-flavor universality and have been proposed as an explanation [22–28] for the deviations from the SM predictions seen by many experiments in measurements of B-meson decays [29–37].

In this note, a search for physics beyond that described in the Standard Model is conducted using events with final states with one or more hadronically decaying tau leptons, one or more b-tagged jets and large missing transverse momentum. This is a signature that is sensitive to models in which the new particles preferentially decay into third-generation SM particles. Two benchmark signal models are studied. The first model considers the production of supersymmetric partner states of the third-generation SM particles, the second model foresees scalar leptoquarks that decay into third-generation SM particles. The full Run-2 dataset of proton–proton (pp) collisions recorded with the ATLAS detector at the Large Hadron Collider (LHC) is analyzed. This dataset corresponds to an integrated luminosity of 139 fb^{-1}, taken from 2015 through 2018, at a center-of-mass energy of $\sqrt{s}$ = 13 TeV.

The investigated SUSY signal model is motivated by gauge-mediated SUSY breaking (GMSB) [38–40] and natural gauge mediation (nGM) [41]. In this R-parity conserving scenario, only three SUSY particles are assumed to be sufficiently light to be relevant: the lighter scalar partner of the top quark $\tilde{t}_1$ (top squark or stop), the lighter scalar partner of the tau lepton $\widetilde{\tau}_1$ (tau slepton or stau), and the spin-3/2 partner of the graviton, the gravitino $\tilde{G}$. The top squark is assumed to be the lightest squark [42, 43] and directly pair-produced through the strong interaction. The gravitino is assumed to be almost massless, making it the lightest SUSY particle (LSP) in this scenario. The search strategy is optimized using a simplified model [44–46] with this limited SUSY particle content, the model parameters being the scalar-fermion masses $m(\tilde{t}_1)$ and $m(\widetilde{\tau}_1)$. The decay chain is illustrated in the left diagram in Fig. 1: a three-body decay proceeding through an off-shell chargino $\tilde{t}_1 \to b\widetilde{\tau}_1\nu_\tau$ followed by $\widetilde{\tau}_1 \to \tau\tilde{G}$. This model is referred to as the "stop-stau" signal model in the following. When the LSP is the gravitino, direct decays of SUSY particles into the gravitino LSP (plus a SM particle) are very unlikely due to its weak coupling, except for the next-to-lightest supersymmetric particle, which in R-parity conserving scenarios has no other option than to eventually decay into the gravitino LSP. Other SUSY models which instead assume the lightest neutralino $\tilde{\chi}_1^0$ to be the LSP are not studied here, as this would favor a high branching fraction of $\tilde{t}_1 \to t\tilde{\chi}_1^0$; this case has been studied elsewhere [47–49].

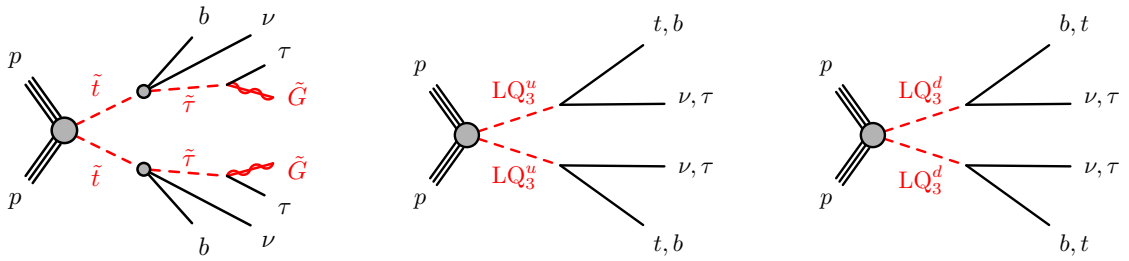

Figure 1: Diagrams illustrating the production and decay of particles considered in the simplified models for the supersymmetric scenario (left) and the scenarios with scalar leptoquarks of charge $\frac{2}{3}e$ (middle) and $-\frac{1}{3}e$ (right).

Previous searches for this model have been conducted by the ATLAS collaboration using 20 fb^{-1} of $\sqrt{s} = 8$ TeV data taken in Run 1 [50] and 36.1 fb^{-1} of $\sqrt{s} = 13$ TeV data taken in Run 2 of the LHC [51]. No significant excess was observed in either of these searches, and thus limits were set on the masses of the top squark and tau slepton. These limits exclude top-squark masses of up to 1.16 TeV and tau-slepton masses of up to 1.0 TeV at the 95 % confidence level. The CMS collaboration has published a related search in a simplified model where the LSP is the lightest neutralino $\tilde{\chi}_1^0$ instead of the gravitino [52]. This search is based on an integrated luminosity of 77.2 fb^{-1} and sets exclusion limits at the 95 % confidence level on the top-squark mass of up to 1.1 TeV for a nearly massless neutralino.

The previous ATLAS Run-2 search in Ref. [51] made use of two event categories: events where one of the two tau leptons decays leptonically and the other hadronically were considered in addition to events where both tau leptons decay hadronically. While the branching fraction is the same for both categories, the leptonic decay of the tau lepton yields one neutrino more, which washes out the kinematic distributions and on average leads to a lower energy fraction carried by the lepton compared to the visible decay products from a hadronic tau-lepton decay. Both effects together significantly reduce the discriminative power of the selection requirements. As the sensitivity of the search is thus dominated by the category where both tau leptons decay hadronically, in this note only events with hadronically decaying tau leptons are considered. These events are split in two event categories (channels): one category selects events with at least two hadronically decaying tau leptons but no lighter leptons, at least one b-jet and large missing transverse momentum $E_{\mathrm{T}}^{\mathrm{miss}}$ (di-tau channel). The other category selects events with exactly one hadronically decaying tau lepton, no electrons or muons, at least two b-jets and large $E_{\mathrm{T}}^{\mathrm{miss}}$ (single-tau channel). The latter channel extends the sensitivity by covering the signal parameter space where the tau slepton is relatively light and one of the soft tau leptons easily escapes detection. Importantly, it also provides good sensitivity to events with pair-produced leptoquarks that decay into third-generation particles, which corresponds to the second benchmark model.

The second benchmark model used for the interpretation of the search results considers pair production of scalar leptoquarks. It assumes that these only couple to third-generation quark–lepton pairs, following the minimal Buchmüller–Rückl–Wyler model [53]. In addition to the coupling to the third fermion generation that is probed in this analysis, leptoquarks would need to have cross-generational couplings in order to explain the anomalies observed in B-meson decays. The couplings in the Yukawa-type interaction of the leptoquarks with the quark–lepton pair are determined by two parameters: a common coupling strength λ and an additional parameter β, with the coupling to a quark and a charged lepton given by $\sqrt{\beta}\lambda$, and the coupling to a quark and a neutrino by $\sqrt{1-\beta}\lambda$. The search is carried out for both up-type leptoquarks with fractional charge $Q(\mathrm{LQ}_3^{\mathrm{u}}) = +2/3e$ and decays $\mathrm{LQ}_3^{\mathrm{u}} \to t\nu_\tau / b\tau$, and down-type leptoquarks with $Q(\mathrm{LQ}_3^{\mathrm{d}}) = -1/3e$ and decays $\mathrm{LQ}_3^{\mathrm{d}} \to b\nu_\tau / t\tau$. The production and decay of the leptoquarks are illustrated in

Fig. 1. The model parameters are the leptoquark mass $m(\mathrm{LQ}_3^{\mathrm{u/d}})$ and the branching fraction $B(\mathrm{LQ}_3^{\mathrm{u/d}} \to q\ell)$ into a quark and a charged lepton, which, except for kinematic effects arising from the mass differences of the decay products, is equal to β. For a branching fraction $B(\mathrm{LQ}_3^{\mathrm{u/d}} \to q\ell) \sim 0.5$, most of the decays of the pair of third-generation leptoquarks yield a final state with one tau lepton, two b-jets and large $E_{\mathrm{T}}^{\mathrm{miss}}$ from the tau neutrino. This signature matches that of the second channel of the search presented in this note, which presents unique coverage of leptoquark masses at $B(\mathrm{LQ}_3^{\mathrm{u/d}} \to q\ell) \sim 0.5$, but also has good sensitivity to a wide range of smaller or larger branching fractions.

The LQ model is the same as was used in a previous ATLAS paper [54] detailing a search for third-generation leptoquarks based on 36.1 fb^{-1} of data taken at $\sqrt{s} = 13$ TeV. This earlier paper comprises a dedicated reoptimisation of the ATLAS search for di-higgs production as well as four reinterpretations of ATLAS SUSY searches, one of which is the previous iteration of the stop-stau search [51]. Leptoquark masses below at least 0.8 TeV are excluded at intermediate values of the branching fraction $B(\mathrm{LQ}_3^{\mathrm{u/d}} \to q\ell)$, with the lower limit increasing at both small and large $B(\mathrm{LQ}_3^{\mathrm{u/d}} \to q\ell)$ up to 0.96 (1.02) TeV at $B(\mathrm{LQ}_3^{\mathrm{u/d}} \to q\ell) = 0$ (1) for down-type (up-type) leptoquarks. Two recent ATLAS searches for top or bottom squark pair production have been reinterpreted in the same up-type or down-type leptoquark model, respectively [47, 55]. Another recent dedicated ATLAS search for pair-produced leptoquarks combines several event categories which all require at least one hadronically decaying tau lepton plus at least one electron or muon [56] and are complementary to the final states considered in this note. It targets the down-type leptoquark model and excludes leptoquark masses up to 1.43 TeV assuming $B(\mathrm{LQ}_3^{\mathrm{u/d}} \to q\ell) = 1$ and up to 1.22 TeV assuming $B(\mathrm{LQ}_3^{\mathrm{u/d}} \to q\ell) = 0.5$. The CMS collaboration has published a search for singly and pair-produced scalar and vector leptoquarks coupling to third-generation fermions based on the full Run-2 dataset [57], excluding scalar pair-produced leptoquarks with masses up to around 1.0 TeV, and several searches for third-generation leptoquarks based on 35.9 fb^{-1} of Run-2 data [58–62].

2 ATLAS detector

The ATLAS experiment [63–65] at the LHC is a multipurpose particle detector with a forward–backward symmetric cylindrical geometry and a near 4π coverage in solid angle.[1] It consists of an inner tracking detector surrounded by a thin superconducting solenoid providing a 2 T axial magnetic field, electromagnetic and hadronic calorimeters, and a muon spectrometer. The inner tracking detector covers the pseudorapidity range $|\eta| < 2.5$. It consists of silicon pixel, silicon microstrip, and transition radiation tracking detectors. Lead/liquid-argon (LAr) sampling calorimeters provide electromagnetic (EM) energy measurements with high granularity. A steel/scintillator-tile hadronic calorimeter covers the central pseudorapidity range ($|\eta| < 1.7$). The endcap and forward regions are instrumented with LAr calorimeters for EM and hadronic energy measurements up to $|\eta| = 4.9$. The muon spectrometer surrounds the calorimeters and is based on three large superconducting air-core toroidal magnets with eight coils each. The muon spectrometer includes a system of precision tracking chambers and fast detectors for triggering. A two-level trigger system is used to select events. The first-level trigger is implemented in hardware and uses a subset of the detector information to accept events at a rate below 100 kHz. This is followed by a software-based

[1] ATLAS uses a right-handed coordinate system with its origin at the nominal interaction point (IP) in the center of the detector and the z-axis along the beam pipe. The x-axis points from the IP to the center of the LHC ring, and the y-axis points upwards. Cylindrical coordinates (r, ϕ) are used in the transverse plane, ϕ being the azimuthal angle around the z-axis. The pseudorapidity is defined in terms of the polar angle θ as $\eta = -\ln\tan(\theta/2)$. Angular distance is measured in units of $\Delta R \equiv \sqrt{(\Delta\eta)^2 + (\Delta\phi)^2}$.

Table 1: Simulated background and signal samples with the corresponding matrix element and parton shower (PS) generators. Also, the cross-section order in α_S used to normalize the event yield and the PDF sets used in the generator and PS simulation are given.

Physics process	Generator	Parton shower	Tune	Cross section	PDF (generator)	PDF (PS)
$t\bar{t}$	Powheg-Box v2 [76–79]	Pythia 8.230 [80]	A14 [71]	NNLO+NNLL [81]	NNPDF3.0NLO [82]	NNPDF2.3LO [74]
Single top	Powheg-Box v2 [77–79, 83]	Pythia 8.230	A14	NLO+NNLL [84–87]	NNPDF3.0NLO	NNPDF2.3LO
V + jets ($V = W, Z$)	Sherpa 2.2.1 [70]	Sherpa 2.2.1	Sherpa default	NNLO [88]	NNPDF3.0NNLO [82]	NNPDF3.0NNLO
Diboson VV ($V = W, Z$)	Sherpa 2.2.1 or 2.2.2 [70]	Sherpa 2.2.1 or 2.2.2	Sherpa default	NLO [89–91]	NNPDF3.0NNLO	NNPDF3.0NNLO
Triboson VVV ($V = W, Z$)	Sherpa 2.2.1	Sherpa 2.2.1	Sherpa default	NLO [89–91]	NNPDF3.0NNLO	NNPDF3.0NNLO
$t\bar{t}+V$ ($V = W, Z$)	MadGraph5_aMC@NLO 2.3.3 [92]	Pythia 8.210 [80]	A14	NLO [92, 93]	NNPDF3.0NLO	NNPDF2.3LO
$t\bar{t}+H$	Powheg-Box v2 [78, 79, 94]	Pythia 8.230	A14	NLO [92, 93]	NNPDF3.0NLO	NNPDF2.3LO
$t\bar{t}+WW$	MadGraph5_aMC@NLO 2.2.2 [92]	Pythia 8.186 [80]	A14	NLO [92]	NNPDF2.3LO	NNPDF2.3LO
$t\bar{t}+WZ$	MadGraph5_aMC@NLO 2.3.3	Pythia 8.212 [80]	A14	NLO [92]	NNPDF3.0NLO	NNPDF2.3LO
tWZ	MadGraph5_aMC@NLO 2.3.3	Pythia 8.212	A14	NLO [92]	NNPDF3.0NLO	NNPDF2.3LO
$tZ, t\bar{t}t, t\bar{t}t\bar{t}$	MadGraph5_aMC@NLO 2.3.3	Pythia 8.230	A14	NLO [92]	NNPDF3.1NLO [82]	NNPDF2.3LO
Stop-stau	MadGraph5_aMC@NLO 2.6.2	Pythia 8.212	A14	approx. NNLO+NNLL [95–98]	NNPDF2.3LO	NNPDF2.3LO
$LQ_3^{u/d}$	MadGraph5_aMC@NLO 2.6.0	Pythia 8.230	A14	approx. NNLO+NNLL [95–98]	NNPDF3.0NLO	NNPDF2.3LO

high-level trigger that reduces the accepted event rate to 1 kHz on average depending on the data-taking conditions.

3 Data and simulated event samples

The dataset used in this analysis was collected with the ATLAS detector in proton–proton collisions provided by the LHC during its second run from 2015 to 2018 at a center-of-mass energy of $\sqrt{s} = 13$ TeV with a minimum separation of 25 ns between consecutive crossings of proton bunches from the two beams. Events are selected with triggers on missing transverse momentum, and data-quality requirements are applied to ensure that all elements of the detectors were operational during data-taking. The total integrated luminosity amounts to 139 fb^{-1} with an uncertainty of 1.7 % [66], obtained using the LUCID-2 detector [67] for the primary luminosity measurements.

Monte Carlo (MC) simulation is used to generate samples of collision events, which model the expected kinematics of the investigated signal and SM background processes. Table 1 gives a detailed summary of the generation of the different MC samples used in the analysis. It lists the generators, the order of the cross-section computation, the parton distribution function (PDF) sets, and the sets of tuned parameters for the parton-shower (tune). For background processes, the detector response is simulated using the full modeling of the ATLAS detector in Geant4 [68], while for the signal samples a faster variant of the simulation is used that relies on a parameterised response of the calorimeters [69]. Except for samples produced with Sherpa [70], which uses a dedicated parton-shower (PS) modeling and parameter tune developed by the Sherpa authors, the parton shower and hadronization simulation for all samples uses the A14 tune [71], and the EvtGen program [72] is used to model the decays of b- and c-hadrons in signal samples and background events. The effect of multiple interactions in the same and neighboring bunch crossings (pile-up) is modeled by overlaying simulated inelastic pp events generated with Pythia8.186 [73] using the NNPDF2.3LO set of PDFs [74] and the A3 tune [75] over the original hard-scattering event. All simulated events are processed with the same trigger, reconstruction and identification algorithms as the data, and are weighted to match the observed distribution of the pile-up in data. Dedicated correction factors are applied to simulation to account for differences in efficiencies and energy calibrations. In this analysis, data-driven methods are applied that improve the modeling of the dominant SM background processes by normalizing their contributions to data. These are described in Section 6.

The production of top-quark pairs, with or without an associated Higgs boson, and of single top quarks in the s- and t-channel or associated with W bosons is simulated with Powheg-Box [76–79], while associated production of top-quark pairs and a vector boson $V = W$ or Z, as well as other top-quark-related processes (later denoted as "other top") with smaller contributions ($t\bar{t} + WW$, $t\bar{t} + WZ$, tWZ, tZ, $t\bar{t}t$ and $t\bar{t}t\bar{t}$) are simulated with MadGraph5_aMC@NLO [92]. The events are interfaced to Pythia [80] to model the parton shower, hadronisation, and underlying event, using the NNPDF2.3LO set of PDFs [74]. The production of single vector boson (V + jets), diboson (VV) and triboson (VVV) events is simulated with Sherpa using the NNPDF3.0NNLO PDF set [82].

Stop-stau signal samples are produced for varying values of $m_{\tilde{t}}$ and $m_{\tilde{\tau}}$. The pair production of top squarks is simulated at leading order with up to two additional partons in MadGraph5_aMC@NLO. For the decays of the SUSY particles, the top squark and the tau slepton, MadSpin [99] is used to preserve spin correlation and finite-width effects. Both decays are assumed to be prompt, i. e. the SUSY particles have a negligible lifetime. The subsequent decays as well as the hadronisation are simulated in Pythia. Cross sections are calculated including approximate next-to-next-to-leading order (NNLO) supersymmetric quantum chromodynamics (QCD) corrections, with resummation of next-to-next-to-leading logarithmic (NNLL) soft gluon terms [95–98]. The matching of matrix element and parton shower was done with the CKKW-L prescription [100, 101], with the matching scale set to one quarter of the top-squark mass.

Simulated events with pair production of scalar third-generation leptoquarks $\mathrm{LQ}_3^{\mathrm{u/d}}$ were generated at next-to-leading order (NLO) in QCD with MadGraph5_aMC@NLO, using the LQ model of Ref. [102] that adds parton showers to previous fixed-order NLO QCD calculations [103, 104], and the NNPDF3.0NLO parton distribution function set with $\alpha_{\mathrm{S}}(m_Z) = 0.118$. MadSpin is used for the prompt decays of the leptoquarks into spin-entangled quark-lepton pairs of the third generation. Parton showering and hadronisation are simulated in Pythia with the NNPDF2.3LO PDF set with $\alpha_{\mathrm{S}}(m_Z) = 0.130$. The leptoquark signal samples are generated for various leptoquark masses $m(\mathrm{LQ}_3^{\mathrm{u/d}})$ and with a fixed value of the parameter $\beta = 0.5$, so that both decays of the leptoquarks, either to a neutrino and a quark or a charged lepton and a quark, are possible. These events can be reweighted to arbitrary branching fractions $B(\mathrm{LQ}_3^{\mathrm{u/d}} \to q\ell)$ to derive the interpretation of the analysis results in the plane of $m(\mathrm{LQ}_3^{\mathrm{u/d}})$ vs. $B(\mathrm{LQ}_3^{\mathrm{u/d}} \to q\ell)$. The coupling parameter λ is set to 0.3, close to the numeric value of the electromagnetic coupling, resulting in a $\mathrm{LQ}_3^{\mathrm{u/d}}$ width of about 0.2 % of its mass [53, 105]. The cross sections for direct top-squark pair production are used for LQ pair-production, as both involve massive, scalar, color-charged particles and the production modes are the same. These cross sections do not include the lepton t-channel contributions possible for LQ pair-production, which are also neglected in Ref. [102] and may lead to corrections at the percent level [106].

4 Event reconstruction

All events are required to have at least one reconstructed interaction vertex with a minimum of two associated tracks with $p_{\mathrm{T}} > 500\,\mathrm{MeV}$. In events with multiple vertices, the one with the highest sum of squared transverse momenta of associated tracks is chosen as the primary vertex (PV) [107].

Jets are reconstructed from particle-flow objects [108] calibrated at the EM scale using the anti-k_t algorithm with a radius parameter of $R = 0.4$. As both signal models predict the production of particles with large masses, only jets in the central region within $|\eta| < 2.8$ are used. The jets are calibrated following the procedure described in Ref. [109] and are required to have $p_{\mathrm{T}} > 20\,\mathrm{GeV}$ and to pass the set of quality criteria defined in Ref. [110]. To suppress jets from pile-up interactions, candidates with $p_{\mathrm{T}} < 60\,\mathrm{GeV}$

and $|\eta| < 2.4$ are required to pass the *Tight* working point of the jet vertex tagger [111]. Selected jets arising from the hadronisation of a bottom quark are flagged as b-jets if they lie within $|\eta| < 2.5$ and are tagged by the `DL1r` algorithm, a multivariate discriminant based on various inputs such as track impact parameters and displaced secondary vertices [112, 113]. The b-tagging algorithm uses a working point with an efficiency of 77 %, with an approximate misidentification probability of 20 % for jets arising from charm quarks, 6.7 % for hadronically decaying τ-leptons, and 0.9 % for light-flavor jets in simulated $t\bar{t}$ events.

Tau leptons which decay leptonically are not identified as such, but are instead reconstructed as a candidate for a prompt electron or muon. Therefore, in the context of reconstructed analysis objects, tau lepton will always refer to a hadronic tau lepton, i. e. a tau lepton that decays hadronically. The visible component of hadronically decaying tau leptons is reconstructed from anti-k_t jets ($R = 0.4$) built from locally calibrated [114] topological clusters, with a distance parameter $R = 0.4$ and requiring $p_{\mathrm{T}} > 10\,\mathrm{GeV}$ and $|\eta| < 2.5$ [115, 116]. The energy calibration applies a pile-up subtraction and a correction to the detector response. Information from the tracking system improves the energy resolution at low p_{T} [116, 117]. Tau-lepton candidates are required to have $p_{\mathrm{T}} > 20\,\mathrm{GeV}$ and lie outside the transition region $1.37 < |\eta| < 1.52$ between the barrel and endcap calorimeters. Furthermore, they must have either one or three charged tracks ("prongs") with a charge sum of ± 1 in units of the elementary charge. A recurrent neural network algorithm [118] distinguishes hadronically decaying tau leptons from quark- and gluon-initiated jets based on a combination of discriminating variables as well as tracking and calorimeter measurements. Its *Medium* working point is used to identify hadronic tau-lepton candidates, with an efficiency of 75 % and 60 % in simulated Drell-Yan events, and background-rejection factors of 35 and 240 in simulated di-jet events, for one-prong and for three-prong decays, respectively. Electrons misidentified as hadronic tau-lepton candidates are rejected using a dedicated boosted decision tree algorithm. Reconstructed tau leptons in simulated events are called "real" tau leptons if they can be geometrically matched to a tau lepton in the MC truth record, otherwise they are referred to as "fake" tau leptons.

As described in Section 5, events with electrons or muons are rejected in the analysis selections, and thus these only enter in the computation of missing transverse momentum and in the overlap-removal procedure, but are not considered otherwise. Electron candidates are reconstructed from energy deposits in the electromagnetic calorimeter that are matched to tracks in the inner detector (ID) [119]. They are required to have $p_{\mathrm{T}} > 10\,\mathrm{GeV}$ and $|\eta| < 2.47$ and pass the *Loose* identification requirement [120]. Muon candidates are reconstructed by combining information from the ID and the muon spectrometer. They are required to have $p_{\mathrm{T}} > 10\,\mathrm{GeV}$ and $|\eta| < 2.7$ and pass the *Medium* identification criteria [121]. The longitudinal impact parameter z_0 of both electron and muon candidates is required to be less than 0.5 mm.

An overlap-removal procedure is applied to all selected objects to resolve ambiguities in the reconstruction in several consecutive steps. First, if two electrons share the same track, the electron with lower transverse momentum is discarded. Tau-lepton candidates overlapping with an electron or a muon within $\Delta R_y < 0.2$ are removed, where $\Delta R_y \equiv \sqrt{(\Delta y)^2 + (\Delta\phi)^2}$ is defined similarly to ΔR but with rapidity y instead of pseudorapidity η for cases where the approximation that the mass can be neglected is not valid. If an electron shares an ID track with a muon, the electron is discarded unless the muon is tagged as a minimum-ionizing particle in the calorimeter, in which case the muon is discarded. Next, jets within $\Delta R_y = 0.2$ of an electron are removed. In order to suppress electrons from semileptonic heavy-flavor decays, electrons within $\Delta R_y = 0.4$ of a jet are removed. Any jet with less than three associated tracks is discarded if a muon is within $\Delta R = 0.2$ or if a muon can be matched to a track associated with the jet. For the same reason as for electrons, muons within $\Delta R_y = 0.4$ of a jet are removed. Lastly, jets within $\Delta R_y = 0.4$ of a tau-lepton candidate are removed.

The missing transverse momentum $\mathbf{E}_{\mathrm{T}}^{\mathrm{miss}}$ is defined as the negative vector sum of the transverse momenta of all calibrated objects mentioned above, photons [120], and an additional soft term including all tracks associated with the PV but not matched to any reconstructed object [122, 123]. The magnitude of $\mathbf{E}_{\mathrm{T}}^{\mathrm{miss}}$ is denoted by $E_{\mathrm{T}}^{\mathrm{miss}}$.

5 Event selection

The analysis covers two different channels, the single-tau and the di-tau channels. In both channels, several different event selections (analysis regions) are defined based on object multiplicities and kinematic variables. All of these event selections start from a common preselection described in the next section. The preselections in the single-tau and in the di-tau channel are identical except for the number of tau leptons and b-tagged jets. The sets of events selected in the two channels are thus mutually exclusive and can therefore be statistically combined, as will be done in the interpretation of the results.

5.1 Preselection

The preselection requirements for the two channels are summarized in Table 2. Events are selected using an $E_{\mathrm{T}}^{\mathrm{miss}}$ trigger. In combination with the requirement of $E_{\mathrm{T}}^{\mathrm{miss}} > 250\,\mathrm{GeV}$, this trigger is fully efficient in the phase space that the analysis targets. As no light leptons are expected from the benchmark signal models when only hadronically decaying tau leptons are considered, events with light leptons are rejected. Events are required to have at least two jets, at least one of which must be b-tagged. Additionally, events in the di-tau channel are required to have at least two reconstructed tau leptons, whereas exactly one tau lepton is required in the single-tau channel and the requirement on the b-tagging multiplicity is tightened to two or more. The tight $E_{\mathrm{T}}^{\mathrm{miss}}$ and b-tagging requirements efficiently suppress multi-jet events such that their contribution to the analysis regions is negligible. This has been verified with dedicated data-driven estimates for both channels.

5.2 Signal regions

Dedicated signal regions are defined for each channel, which have been optimized individually by maximizing the estimated discovery significance [124] for benchmark signal models close to the previous exclusion contours. The selection requirements for the signal regions are explained in the following, and a

Table 2: Preselection of the di-tau and single-tau channels.

Di-tau preselection	Single-tau preselection
$E_{\mathrm{T}}^{\mathrm{miss}}$-trigger fired and $E_{\mathrm{T}}^{\mathrm{miss}} > 250\,\mathrm{GeV}$	
No light leptons (e/μ)	
At least two jets	
At least one b-tagged jet	
At least two hadronic tau candidates	Exactly one hadronic tau candidate
	At least two b-tagged jets

summary is included in the overview tables of the analysis regions in Table 3 for the di-tau channel and Table 4 for the single-tau channel. The signal region (SR) in the di-tau channel targets stop-stau signal models with low to modest mass differences between the top squark and the tau slepton. This SR is not used for the leptoquark model, as the final states for that model at $\beta = 0.5$ on average only have one tau lepton, and the case of $\beta = 1.0$ is not in the scope of this note. The single-tau channel employs two signal regions: a one-bin SR for the model-independent fit, and a multi-bin SR for the model-dependent fit, as will be discussed in Section 8. Both signal regions in this channel are optimized simultaneously for stop-stau signals with a large mass difference between the top squark and the tau slepton as well as for the leptoquark benchmark signal model.

Di-tau channel

The most discriminating variable in the di-tau channel is the stransverse mass variable [125, 126], which by itself already provides good separation between the signal and the background. The stransverse mass m_{T2} is a generalization of the transverse mass m_{T}, which is computed as $m_{\mathrm{T}}(\mathbf{p}_{\mathrm{T}}, \mathbf{E}_{\mathrm{T}}^{\mathrm{miss}})^2 = 2\, p_{\mathrm{T}}\, E_{\mathrm{T}}^{\mathrm{miss}} \left(1 - \cos\Delta\phi(\mathbf{p}_{\mathrm{T}}, \mathbf{E}_{\mathrm{T}}^{\mathrm{miss}})\right)$, from the transverse momentum of some given particle and the missing transverse momentum. It generalizes the transverse mass for event topologies where two identical particles each symmetrically decay into a visible and an invisible product. In this case the individual transverse momenta of the invisible particles can no longer be directly approximated by the measured missing transverse momentum, as the information about their individual contributions to the missing transverse momentum is lost. For the two leading tau leptons, i. e. the two tau leptons with the largest and second-largest transverse momentum, $m_{\mathrm{T2}}(\tau_1, \tau_2)$ is computed as

$$m_{\mathrm{T2}}(\tau_1, \tau_2) = \min_{\mathbf{q}_{\mathrm{T}}^a + \mathbf{q}_{\mathrm{T}}^b = \mathbf{E}_{\mathrm{T}}^{\mathrm{miss}}} \left(\max \left[m_{\mathrm{T}}(\mathbf{p}_{\mathrm{T}}^{\tau_1}, \mathbf{q}_{\mathrm{T}}^a), m_{\mathrm{T}}(\mathbf{p}_{\mathrm{T}}^{\tau_2}, \mathbf{q}_{\mathrm{T}}^b) \right] \right), \tag{1}$$

where a and b refer to two invisible particles assumed to be produced with transverse momentum $\mathbf{q}_{\mathrm{T}}^{a,b}$. The minimum is taken over all possible assignments to $\mathbf{q}_{\mathrm{T}}^{a,b}$ that sum to the measured $\mathbf{E}_{\mathrm{T}}^{\mathrm{miss}}$. The masses of the invisible particles are free parameters and are set to zero. For the dominant top-quark related backgrounds, the $m_{\mathrm{T2}}(\tau_1, \tau_2)$ distribution features an endpoint near the W-boson mass. By placing a lower bound at 70 GeV most of this background can be removed, while efficiently selecting signal events, for which the $m_{\mathrm{T2}}(\tau_1, \tau_2)$ distribution exhibits a tail towards much higher values. The sensitivity is further enhanced by raising the lower bound on $E_{\mathrm{T}}^{\mathrm{miss}}$ to 280 GeV and requiring the two leading tau leptons to carry electric charges with opposite signs, a criterion later denoted as $OS(\tau_1, \tau_2) = 1$.

Single-tau channel

Both signal regions in the single-tau channel have a lower bound on $E_{\mathrm{T}}^{\mathrm{miss}}$ at 280 GeV and on the sum of the transverse masses of the b-jets, $\sum m_{\mathrm{T}}(b_{1,2}) = m_{\mathrm{T}}(b_1) + m_{\mathrm{T}}(b_2)$, at 700 GeV. In this expression and the following, $m_{\mathrm{T}}(A)$ for a given particle A should be read as $m_{\mathrm{T}}(A) \equiv m_{\mathrm{T}}(\mathbf{p}_{\mathrm{T}}^A, \mathbf{E}_{\mathrm{T}}^{\mathrm{miss}})$. The one-bin SR requires $m_{\mathrm{T}}(\tau) > 300$ GeV and $s_{\mathrm{T}} > 800$ GeV, where s_{T} is defined as the scalar sum of transverse momenta of the tau lepton and the two leading jets, $s_{\mathrm{T}} = p_{\mathrm{T}}(\tau) + p_{\mathrm{T}}(\mathrm{jet}_1) + p_{\mathrm{T}}(\mathrm{jet}_2)$. While both the stop-stau and $\mathrm{LQ}_3^{\mathrm{u/d}}$ signals show relatively similar behavior in most kinematic variables, their $p_{\mathrm{T}}(\tau)$ distributions differ. This is due to the large mass difference of the stop-stau target scenario, so that the tau leptons are softer compared to those produced in the $\mathrm{LQ}_3^{\mathrm{u/d}}$ decay. To account for the different shapes of the transverse momenta of the tau leptons, the second SR is defined with three bins in $p_{\mathrm{T}}(\tau)$. The first

two $p_{\mathrm{T}}(\tau)$ bins cover 50 to 100 GeV and 100 to 200 GeV, and the last bin everything beyond 200 GeV. To maintain a sufficiently large number of events in each of the three $p_{\mathrm{T}}(\tau)$ bins, two selection requirements are loosened with respect to the one-bin SR: the minimum $m_{\mathrm{T}}(\tau)$ requirement is lowered to 150 GeV, and the minimum s_{T} requirement to 600 GeV. As the one-bin SR is a subset of the multi-bin SR, they cannot be combined in the statistical interpretation of the results discussed in Section 8. A multi-bin SR based on s_{T} instead of $p_{\mathrm{T}}(\tau)$ has also been tested, but was found to have lower sensitivity.

6 Background estimation

The background in the signal regions is dominated by $t\bar{t}$ and single-top production, which can yield events with a final state similar to the signal processes. For these background processes dedicated control regions are defined. Top-quark production can contribute to the background in different ways. Events with $t\bar{t}$ production, where both W bosons arising from the top-quark decay into a hadronic tau lepton, have two real tau leptons. This process, denoted by $t\bar{t}$ (2 real τ), contributes to the di-tau channel if both hadronic tau leptons are correctly identified. If instead only one of the W bosons from the $t\bar{t}$ system gives a hadronic tau lepton which is correctly identified, and the second W boson decays hadronically, the resulting jet from the second W-boson decay can be misidentified as a tau lepton, and such an event can then still pass the di-tau channel selection criteria. While the mis-identification probability is of the order of a few percent, the larger branching fraction of hadronic W decays and the less pronounced endpoint in the $m_{\mathrm{T2}}(\tau_1, \tau_2)$ distribution for $t\bar{t}$ events with one real and one fake tau lepton still leads to a significant contribution in the di-tau channel. This type of event can also enter the single-tau channel selection, if the jet from the second W boson is not misidentified as a tau candidate. Di-tau $t\bar{t}$ events in which only one of the two identified tau leptons is real, and single-tau $t\bar{t}$ events with one real tau lepton are referred to as $t\bar{t}$ (1 real τ) events. Lastly, fully hadronic $t\bar{t}$ decays, without any real tau leptons that pass the selections in either the single-tau or di-tau channel are referred to as $t\bar{t}$-fake events. Due to their different kinematics, the simulated $t\bar{t}$ events are split into these three types of events, $t\bar{t}$ (2 real τ), $t\bar{t}$ (1 real τ), and $t\bar{t}$-fake, and treated as separate background components in the following.

Sub-dominant contributions to the SM background arise from singly produced vector bosons (W + jets and Z + jets events) and production of vector bosons in association with top-quark pairs ($t\bar{t} + V$). In addition, multi-boson production, $t\bar{t}$ production in association with a Higgs boson ($t\bar{t} + H$) and other top-related processes yield small contributions. These sub-dominant processes are normalized according to their cross sections and the integrated luminosity measured in data.

The normalization of the MC predictions is extracted in a simultaneous maximum-likelihood fit to the observed data in the control regions (CRs). This fit, where no signal contributions are included, is referred to as the background-only fit. The CRs are designed to be enriched in a given background process and to be kinematically as similar to the SRs as possible, while maintaining sufficient purity, a high enough event yield and keeping the signal contamination negligible. In addition to the data yields in the CRs, the expected yields and statistical and systematic uncertainties from MC simulation, described in Section 7, are input to the background-only fit. The yields obtained from the background-only fit can then be extrapolated to dedicated validation regions (VRs) to assess the accuracy of the background estimate. All CR, VR and SR selections are mutually exclusive so that they are statistically independent as required for the fit. The CR and VR selections are introduced in Sections 6.1 and 6.2 for the di-tau and single-tau channel, respectively. The signal regions are used for limit setting as discussed in Section 8. All fit setups are implemented using the HistFitter framework [127].

Table 3: Definitions of the $t\bar{t}$ control and validation regions and the signal region in the di-tau channel. A dash signifies that no requirement on the given variable is applied, while brackets indicate an allowed range for the variable. These requirements extend those of the di-tau preselection from Table 2.

Variable	CR $t\bar{t}$ (2 real τ)	CR $t\bar{t}$ (1 real τ)	VR $t\bar{t}$ (2 real τ)	VR $t\bar{t}$ (1 real τ)	SR
$E_{\mathrm{T}}^{\mathrm{miss}}$	—	—	—	—	$> 280\,\mathrm{GeV}$
$OS(\tau_1, \tau_2)$	1	—	1	—	1
$m_{\mathrm{T2}}(\tau_1, \tau_2)$	$< 35\,\mathrm{GeV}$	$< 35\,\mathrm{GeV}$	$[35, 70]\,\mathrm{GeV}$	$[35, 70]\,\mathrm{GeV}$	$> 70\,\mathrm{GeV}$
$m_{\mathrm{vis}}(\tau_1, \tau_2)$	$> 50\,\mathrm{GeV}$	$> 50\,\mathrm{GeV}$	—	—	—
$m_{\mathrm{T}}(\tau_1)$	$> 50\,\mathrm{GeV}$	$< 50\,\mathrm{GeV}$	$> 70\,\mathrm{GeV}$	$< 70\,\mathrm{GeV}$	—

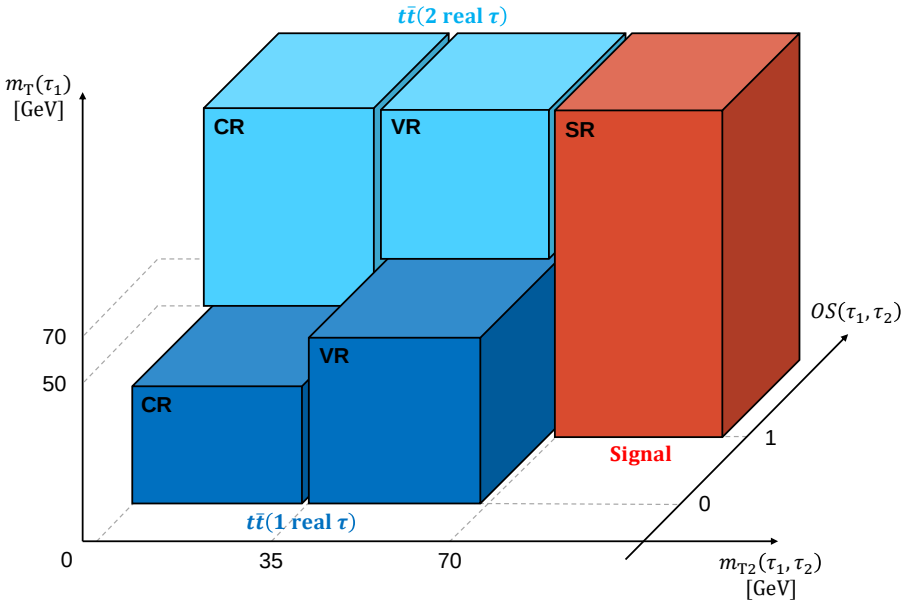

Figure 2: Overview of the selections defining the control, validation and signal regions in the di-tau channel in the phase-space spanned by the variables $m_{\mathrm{T2}}(\tau_1, \tau_2)$, $m_{\mathrm{T}}(\tau_1)$, and $\mathrm{OS}(\tau_1, \tau_2)$, where $\mathrm{OS}(\tau_1, \tau_2) = 1$ means that the reconstructed charge of the two leading tau leptons has opposite sign. In addition to these variables $E_{\mathrm{T}}^{\mathrm{miss}} > 280\,\mathrm{GeV}$ is required for the signal region, and $m_{\mathrm{vis}}(\tau_1, \tau_2) > 50\,\mathrm{GeV}$ for the control regions. The complete definitions are summarized in Table 3.

6.1 Di-tau channel

Table 3 summarizes the definitions of the control, validation and signal-region selections in the di-tau channel. One control region and one validation region are defined in this channel for each of the $t\bar{t}$ (2 real τ) and $t\bar{t}$ (1 real τ) processes. Their location in the phase-space spanned by $m_{\mathrm{T2}}(\tau_1, \tau_2)$, $m_{\mathrm{T}}(\tau_1)$, and $OS(\tau_1, \tau_2)$ is illustrated in Fig. 2. The CRs and VRs sit in the $m_{\mathrm{T2}}(\tau_1, \tau_2)$ sideband below 70 GeV, above which the SR is located, and are divided at 35 GeV.

Top-quark pair-production events in which only one of the W bosons decays leptonically, with one real tau lepton and one fake tau lepton, feature an endpoint in the m_{T} distribution of the real tau lepton near the W mass. The reason is that the dominant source of $E_{\mathrm{T}}^{\mathrm{miss}}$ is the tau neutrino from the W decay. By contrast, for $t\bar{t}$ events with two real tau leptons, two tau neutrinos contribute to the $E_{\mathrm{T}}^{\mathrm{miss}}$ and there is no distinct

endpoint in m_{T}. This difference in the shapes of the m_{T} distributions is exploited in the selection of $t\bar{t}$ (2 real τ) and $t\bar{t}$ (1 real τ) events. In the majority of $t\bar{t}$ (1 real τ) events in the di-tau channel, the real tau lepton corresponds to the leading reconstructed tau lepton. A requirement on $m_{\mathrm{T}}(\tau_1)$ at 50 (70) GeV is thus used to separate the $t\bar{t}$ (2 real τ) CR (VR) from the $t\bar{t}$ (1 real τ) CR (VR). By requiring the leading and subleading tau lepton in the $t\bar{t}$ (2 real τ) CR and VR selections to carry electric charges of opposite sign, $OS(\tau_1, \tau_2) = 1$, the purity is further increased. In addition, a lower bound on the invariant mass of the two tau leptons computed from the visible decay products, $m_{\mathrm{vis}}(\tau_1, \tau_2)$, at 50 GeV is applied to reduce the contribution from Z + jets events.

Distributions of the main discriminating variables $m_{\mathrm{T2}}(\tau_1, \tau_2)$ and $E_{\mathrm{T}}^{\mathrm{miss}}$ in the control and validation regions of the di-tau channel are shown in Fig. 3. The predictions for the top-quark backgrounds are scaled with the normalization factors obtained from the background-only fit. From the plots it can be seen that the background model describes the data very well.

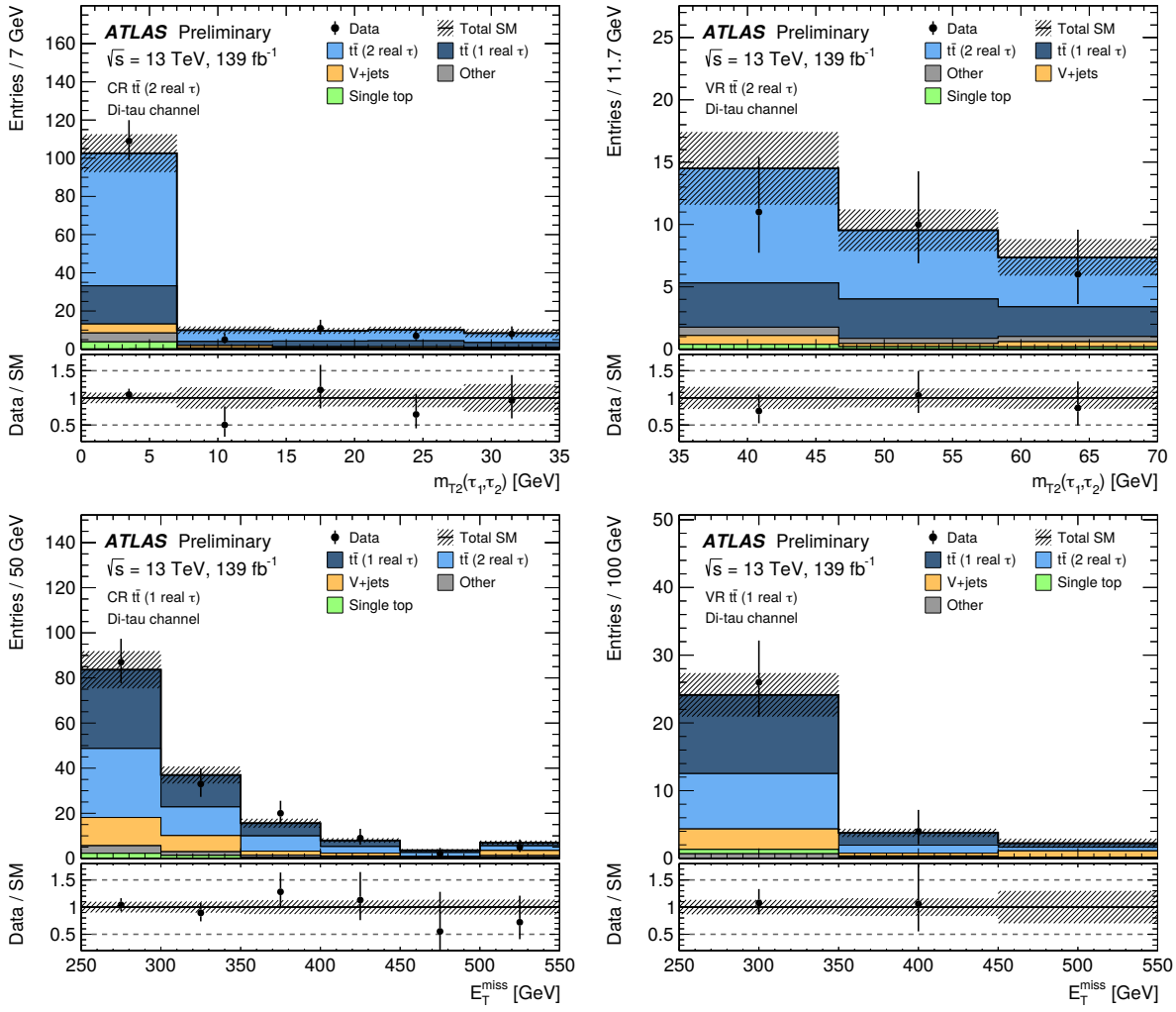

Figure 3: Distributions of $m_{\mathrm{T2}}(\tau_1, \tau_2)$ and $E_{\mathrm{T}}^{\mathrm{miss}}$ in the di-tau channel. The left-hand plots show the control regions and the right-hand plots the validation regions, with $m_{\mathrm{T2}}(\tau_1, \tau_2)$ in the $t\bar{t}$ (2 real τ) CR and VR in the top row and $E_{\mathrm{T}}^{\mathrm{miss}}$ in the $t\bar{t}$ (1 real τ) CR and VR in the bottom row. The CRs and VRs have different requirements on the transverse mass $m_{\mathrm{T}}(\tau_1)$. The stacked histograms show the various SM background contributions. The hatched band indicates the total statistical and systematic uncertainty of the SM background. The $t\bar{t}$ (2 real τ) and $t\bar{t}$ (1 real τ) as well as the single-top background contributions are scaled with the normalization factors obtained from the background-only fit. Minor backgrounds are grouped together and denoted as "Other". This includes $t\bar{t}$-fake, $t\bar{t} + X$, multiboson, and other top. The rightmost bin includes the overflow.

6.2 Single-tau channel

For the two dominant processes in the single-tau channel, $t\bar{t}$ production with one real tau lepton and single-top production, again two pairs of control and validation regions are defined. The definitions are illustrated in Fig. 4 and summarized in Table 4. In contrast to the di-tau CRs and VRs, the larger available number of events in the single-tau channel allows the same lower bound on $E_{\mathrm{T}}^{\mathrm{miss}}$ to be used in the CR and VR selections as for the SR. The $t\bar{t}$ (1 real τ) control and validation regions in the single-tau channel are placed in the $\sum m_{\mathrm{T}}(b_{1,2})$ sideband between 600 and 700 GeV. The control region is located in the s_{T} window from 500 to 600 GeV, and the validation region covers the range above 600 GeV. The normalization of the $t\bar{t}$ (1 real τ) process is obtained from a simultaneous fit of both control regions for this process, one from each channel. The CR and VR for the single-top background sit in the $m_{\mathrm{T}}(\tau)$ window from 0 to 50 GeV and 50 to 150 GeV, respectively. Additionally, lower bounds on $\sum m_{\mathrm{T}}(b_{1,2})$ at 800 GeV and on $p_{\mathrm{T}}(\tau)$ at > 80 GeV increase the purity of both the single-top CR and VR. Events from $t\bar{t}$ (1 real τ) are less likely to fulfill the $p_{\mathrm{T}}(\tau)$ requirement, which favors high-energetic decay products. They also tend

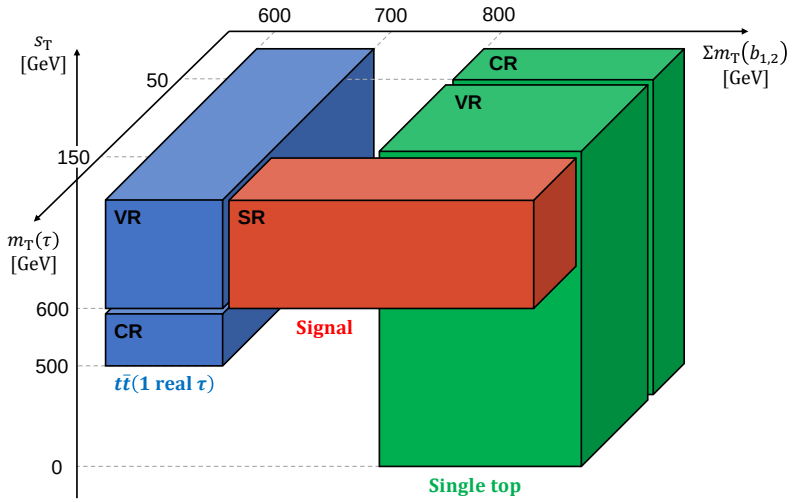

Figure 4: Overview of the selections defining the control, validation and multi-bin signal region in the single-tau channel in the phase-space spanned by the variables $\sum m_{\mathrm{T}}(b_{1,2})$, $m_{\mathrm{T}}(\tau)$ and s_{T}. In addition to these variables, $E_{\mathrm{T}}^{\mathrm{miss}} > 280$ GeV is required for the signal region, and $p_{\mathrm{T}}(\tau_1) > 80$ GeV for the single-top control region and validation regions. The complete definitions are summarized in Table 4.

Table 4: Definitions of the $t\bar{t}$ (1 real τ) and single-top control and validation regions and the signal region in the single-tau channel. A dash signifies that no requirement on the given variable is applied, while brackets indicate an allowed range for the variable. In the last column, round brackets enclose the values and ranges used for the multi-bin SR. The binning in $p_{\mathrm{T}}(\tau)$ of the multi-bin SR, abbreviated with "binned", is $[50, 100]$, $[100, 200]$, and > 200 GeV. These requirements extend those of the single-tau preselection from Table 2.

Variable	CR $t\bar{t}$ (1 real τ)	CR single top	VR $t\bar{t}$ (1 real τ)	VR single top	SR
$E_{\mathrm{T}}^{\mathrm{miss}}$	> 280 GeV	> 280 GeV	> 280 GeV	> 280 GeV	> 280 GeV
s_{T}	$[500, 600]$ GeV	—	> 600 GeV	—	$> 800(600)$ GeV
$\sum m_{\mathrm{T}}(b_{1,2})$	$[600, 700]$ GeV	> 800 GeV	$[600, 700]$ GeV	> 800 GeV	> 700 GeV
$m_{\mathrm{T}}(\tau)$	—	< 50 GeV	—	$[50, 150]$ GeV	$> 300(150)$ GeV
$p_{\mathrm{T}}(\tau)$	—	> 80 GeV	—	> 80 GeV	— (binned)

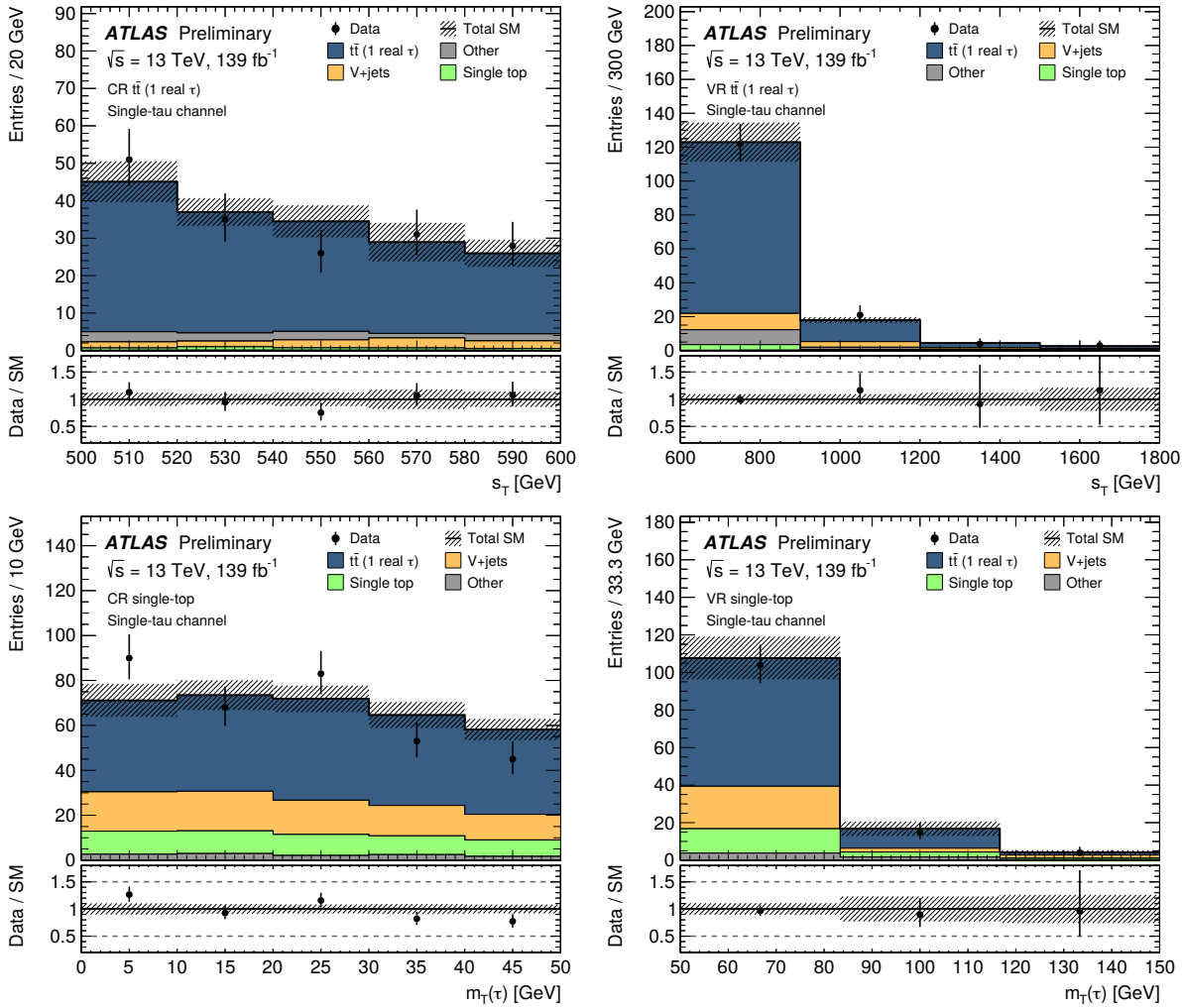

Figure 5: Distributions of s_{T} and $m_{\mathrm{T}}(\tau)$ in the control regions and the validation regions of the single-tau channel. The top row shows s_{T} in the $t\bar{t}$ (1 real τ) CR (left) and $t\bar{t}$ (1 real τ) VR (right), the bottom row shows $m_{\mathrm{T}}(\tau)$ in the single-top CR (left) and single-top VR (right). The stacked histograms show the various SM background contributions. The hatched band indicates the total statistical and systematic uncertainty of the SM background. The $t\bar{t}$ (1 real τ) and single-top background contributions are scaled with the normalization factors obtained from the background-only fit. Minor backgrounds are grouped together and denoted as "Other". This includes $t\bar{t}$-fake, $t\bar{t}+X$, multiboson, and other top. The rightmost bin includes the overflow.

to have lower $\sum m_{\mathrm{T}}(b_{1,2})$, as the transverse mass computed for the sub-leading b-jet has a quite distinct endpoint around the top-quark mass.

Figure 5 shows the distribution of s_{T} and $m_{\mathrm{T}}(\tau)$ in the $t\bar{t}$ (1 real τ) CR and VR and in the single-top CR and VR of the single-tau channel. The predictions for the top-quark backgrounds are scaled with the normalization factors obtained from the background-only fit. These are consistent with unity for the $t\bar{t}$ (2 real τ) and $t\bar{t}$ (1 real τ) backgrounds, but much smaller than one for the single-top background as discussed further in Section 8. Therefore, the contribution of scaled single-top events to the single-top CR and VR in the figure is very low, whereas it is 43 % before applying the normalization factors. From the plots it can be seen that the background model describes the data very well.

Table 5: Relative systematic uncertainties on the estimated number of background events in the signal regions. In the lower part of the table, a breakdown of the total uncertainty into different categories is given. For the multi-bin SR, the breakdown refers to the integral over all three $p_{\mathrm{T}}(\tau)$ bins. As the individual uncertainties are correlated, they do not add in quadrature to equal the total background uncertainty.

Systematic uncertainty	Di-tau SR	Single-tau one-bin SR	Single-tau multi-bin SR
Total	25 %	17 %	17 %
Jet-related	19 %	4.2 %	3.9 %
Tau-related	4.7 %	5.5 %	4.3 %
Other experimental	3.7 %	1.0 %	0.8 %
Theoretical modeling	13 %	17 %	19 %
MC statistics	12 %	7.5 %	4.4 %
Normalization factors	8.8 %	15 %	16 %
Luminosity	0.8 %	0.5 %	0.4 %

7 Systematic uncertainties

The expected yields for signal and background processes are subject to experimental and theoretical systematic uncertainties. They are treated as nuisance parameters with Gaussian probability densities in the likelihood fits.

Experimental uncertainties comprise systematic uncertainties in the reconstruction, identification, calibration and corrections performed for the physics objects used in the analysis. Energy resolution and calibration uncertainties apply to all objects. For tau leptons additional experimental systematic uncertainties arise from the reconstruction and identification efficiencies. As events with electrons and muons are rejected at preselection level, the related uncertainties in the reconstruction and identification are negligible in the analysis regions. For jets, additional uncertainties from the pileup subtraction, pseudorapidity intercalibration, flavor composition, and punch-through effects, as well as uncertainties in the flavor-tagging and jet-vertex tagging efficiencies are considered. Systematic uncertainties affecting the energy or momentum of calibrated objects are propagated to the $E_{\mathrm{T}}^{\mathrm{miss}}$ calculation, and an additional uncertainty due to the contribution of the soft-track term is considered. Common sources of experimental uncertainty are assumed to be correlated across all regions and between the background processes and the signal.

Uncertainties in the renormalisation and factorization scales are considered for all major background processes by separately varying the scales μ_{r} and μ_{f} up and down by a factor of two. Additionally, PDF and α_{S} uncertainties are considered following the PDF4LHC15 prescription [128]. The PDF uncertainty is evaluated as the root mean square of a set of 100 variations, and the α_{S} uncertainty is derived by taking the average difference between the up and down variations. Additional initial-state and final-state radiation uncertainties are considered for the $t\bar{t}$ and single-top processes by varying generator settings, such as the simultaneous μ_{r} and μ_{f} variation and eigenvariations of the A14 tune [71]. Furthermore, theoretical uncertainties due to the hard-scatter and parton-shower simulation are estimated by comparing the corresponding nominal yields against those predicted with alternative generators, i. e. Powheg versus aMC@NLO and Pythia 8 versus Herwig 7, respectively. The impact of the interference between single-top Wt and $t\bar{t}$ production is estimated by comparing samples produced with the nominal diagram-removal scheme to alternative samples generated with the diagram-subtraction scheme [129]. For V + jets, additional uncertainties related to the resummation and CKKW matching scales [130, 131] are considered. Uncertainties in the cross section and in the integrated luminosity of the data are applied for all simulated

processes except for $t\bar{t}$ with one or two real tau leptons and single-top quark production, which are normalized to data.

Table 5 summarizes the total systematic uncertainties on the background expectation in the signal regions. In the di-tau SR the largest sources of experimental uncertainty are the uncertainties in the jet energy resolution, whereas hard-scatter and parton-shower uncertainties dominate the uncertainty on the theoretical modeling. For the one-bin and multi-bin SRs in the single-tau channel, the theoretical uncertainties on the $t\bar{t}$ final state radiation and interference with the Wt process take the leading role.

For the theoretical uncertainties on the signal acceptance an estimate of 20 % is used, which is derived from a study of the impact of variations in the renormalisation and factorization scales, the radiation and merging scales, the PDF, and the α_S value for several stop-stau and $LQ_3^{u/d}$ signal points. Uncertainties on the signal production cross section are considered separately in the interpretation of the results discussed in Section 8.

8 Results

The predictions of the event yields from SM background processes obtained from the background-only fit to the control regions, as described in Section 6, and the observed data are shown in Table 6 for the signal regions in the di-tau and single-tau channel. Events with pair-produced top-quarks make up the largest contribution in all signal regions. The normalization factors obtained from the background-only fit are $0.93^{+0.32}_{-0.23}$ for the $t\bar{t}$ (2 real τ) background, $0.84^{+0.21}_{-0.17}$ for $t\bar{t}$ (1 real τ), and $0.18^{+0.19}_{-0.16}$ for single-top production. The normalization factor for single-top production is significantly smaller than one and strongly depends on

Table 6: Observed event yields in data ("Observed") and expected event yields for SM background processes obtained from the background-only fit ("Total bkg." and rows below) in the signal regions of the di-tau and single-tau channels. The quoted uncertainties include both the statistical and systematic uncertainties and are truncated at zero. By construction no $t\bar{t}$ (2 real τ) events can pass the selections in the single-tau channel. As the individual uncertainties are correlated, they do not add in quadrature to equal the total background uncertainty.

	Di-tau SR	Single-tau SR (one-bin)	Single-tau SR (binned in $p_T(\tau)$)		
			[50, 100] GeV	[100, 200] GeV	> 200 GeV
Observed	2	6	8	6	2
Total bkg.	4.1 ±1.0	3.23 ±0.55	10.1 ±1.8	5.1 ±1.1	2.05 ±0.64
$t\bar{t}$ (2 real τ)	0.81 ±0.71	—	—	—	—
$t\bar{t}$ (1 real τ)	0.82 ±0.27	1.20 ±0.30	4.8 ±1.2	2.69 ±0.88	0.64 ±0.29
$t\bar{t}$-fake	0.51 ±0.15	0.69 ±0.15	2.83 ±0.87	0.66 ±0.17	0.185 ±0.072
Single top	0.03 $\pm^{0.10}_{0.03}$	0.39 $\pm^{0.45}_{0.39}$	0.85 $\pm^{0.86}_{0.85}$	0.54 ±0.54	0.57 ±0.56
W + jets	0.08 $\pm^{0.11}_{0.08}$	0.35 ±0.16	0.34 ±0.12	0.64 ±0.24	0.37 ±0.12
Z + jets	0.35 ±0.14	0.187 ±0.054	0.275 ±0.081	0.043 ±0.022	0.123 ±0.048
Multiboson	0.48 ±0.21	0.085 ±0.037	0.163 ±0.037	0.111 ±0.030	0.030 $\pm^{0.032}_{0.030}$
$t\bar{t}+V$	0.60 ±0.15	0.242 ±0.064	0.65 ±0.16	0.31 ±0.12	0.092 ±0.035
$t\bar{t}+H$	0.28 $\pm^{0.29}_{0.28}$	0.039 $\pm^{0.040}_{0.039}$	0.10 ±0.10	0.060 $\pm^{0.061}_{0.060}$	0.028 $\pm^{0.029}_{0.028}$
Other top	0.122 ±0.067	0.043 ±0.022	0.096 ±0.074	0.091 ±0.049	0.0120 ±0.0084

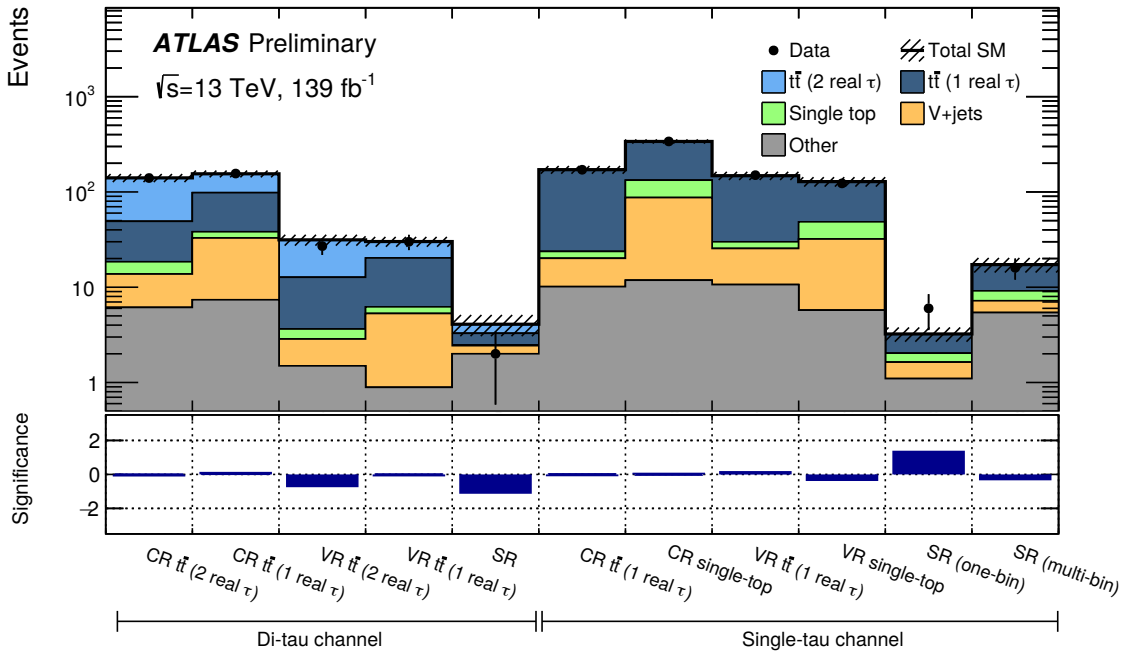

Figure 6: Comparison of expected and observed event yields (top panel) and the significance of their discrepancy (bottom panel) for all analysis regions of the di-tau and single-tau channel. The hatched band in the top panel indicates the combined statistical and systematic uncertainties in the expected SM background. The $t\bar{t}$ (2 real τ) and $t\bar{t}$ (1 real τ) as well as the single-top background contributions are scaled with the normalization factors obtained from the background-only fit. Minor backgrounds are grouped together and denoted as "Other". This includes $t\bar{t}$-fake, $t\bar{t}+X$, multiboson, and other top. The entries in the column labeled "SR (multi-bin)" are the sum of the three bins of the multi-bin signal-region.

how the interference between single-top production at next-to-leading order and leading-order $t\bar{t}$ production is handled [129, 132, 133]. The value 0.18 is obtained from the samples generated with the nominal diagram-removal scheme. The alternative diagram-subtraction scheme gives a normalization factor larger than one with very large uncertainties due to the much smaller yields and thus insufficient purity in the control region. The difference in the CR yields can be attributed to the much softer b-jet distribution for the diagram-subtraction scheme. However, the shape of $m_{\mathrm{T}}(\tau_1)$, in which the extrapolation from the control to the signal region is done, agrees very well between both schemes, giving confidence in the validity of the extrapolation. The difference between both interference schemes is taken into account as a systematic uncertainty.

No significant excess of the data above the SM expectation is observed in any of the signal regions. The largest excursions from the expected yields are a deficit with a significance of $1.0\,\sigma$ in the signal region of the di-tau channel and an excess with a significance of $1.3\,\sigma$ in the one-bin signal region of the single-tau channel, computed with the approximate formulae from Ref. [124]. The excess is not present, however, in the binned signal region of the single-tau channel. Figure 6 compares the observed data yields with the expected background predictions for all event selections of the analysis. The entries in the right-most column of the plot are the sum of the three bins of the multi-bin signal-region in the single-tau channel, labeled "SR (multi-bin)". Figure 7 shows several kinematics distributions of the SM background expectation, and compares them with the distributions expected for the several benchmark signal models and the observed data in the di-tau and single-tau signal regions.

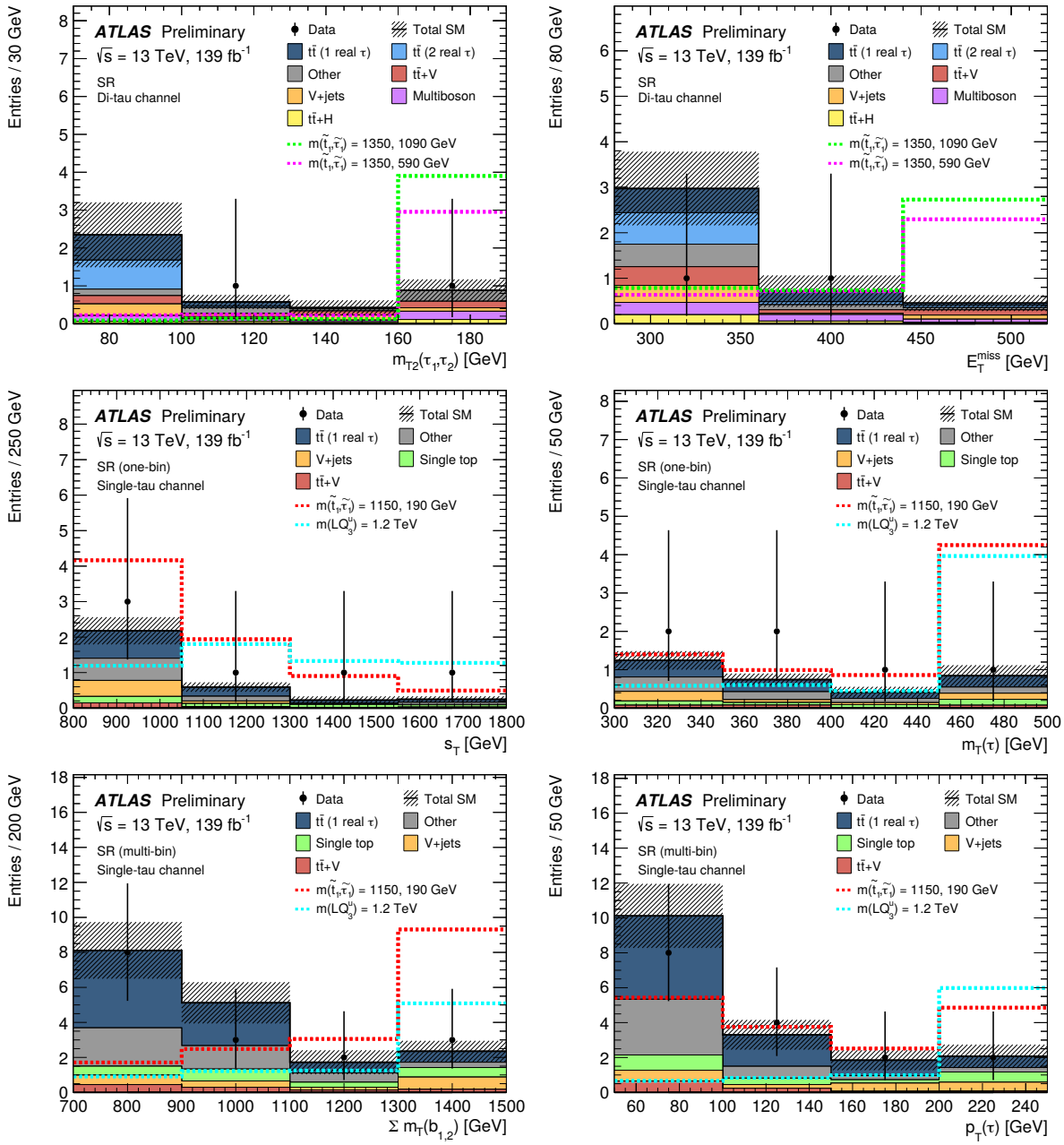

Figure 7: Distributions of $m_{\mathrm{T2}}(\tau_1, \tau_2)$ and $E_{\mathrm{T}}^{\mathrm{miss}}$ in the di-tau SR (top), of s_{T} and $m_{\mathrm{T}}(\tau)$ in the single-tau one-bin SR (middle) and of $\sum m_{\mathrm{T}}(b_{1,2})$ and $p_{\mathrm{T}}(\tau)$ in the single-tau $p_{\mathrm{T}}(\tau)$-binned SR (bottom). The stacked histograms show the various SM background contributions. The hatched band indicates the total statistical and systematic uncertainty of the SM background. The $t\bar{t}$ (2 real τ) and $t\bar{t}$ (1 real τ) as well as the single-top background contributions are scaled with the normalization factors obtained from the background-only fit. Minor backgrounds are grouped together and denoted as "Other". This includes $t\bar{t}$-fake, single top, and other top (di-tau channel) or $t\bar{t}$-fake, $t\bar{t}+H$, multiboson, and other top (single-tau channel) . The overlaid dotted lines show the additional contributions for signal scenarios close to the expected exclusion contour with the particle type and the mass parameters for the simplified models indicated in the legend. For the leptoquark signal model, the parameter β here is set to 0.5, and the shape for $\mathrm{LQ}_3^{\mathrm{d}}$ (not shown) is similar to that of $\mathrm{LQ}_3^{\mathrm{u}}$. The rightmost bin includes the overflow.

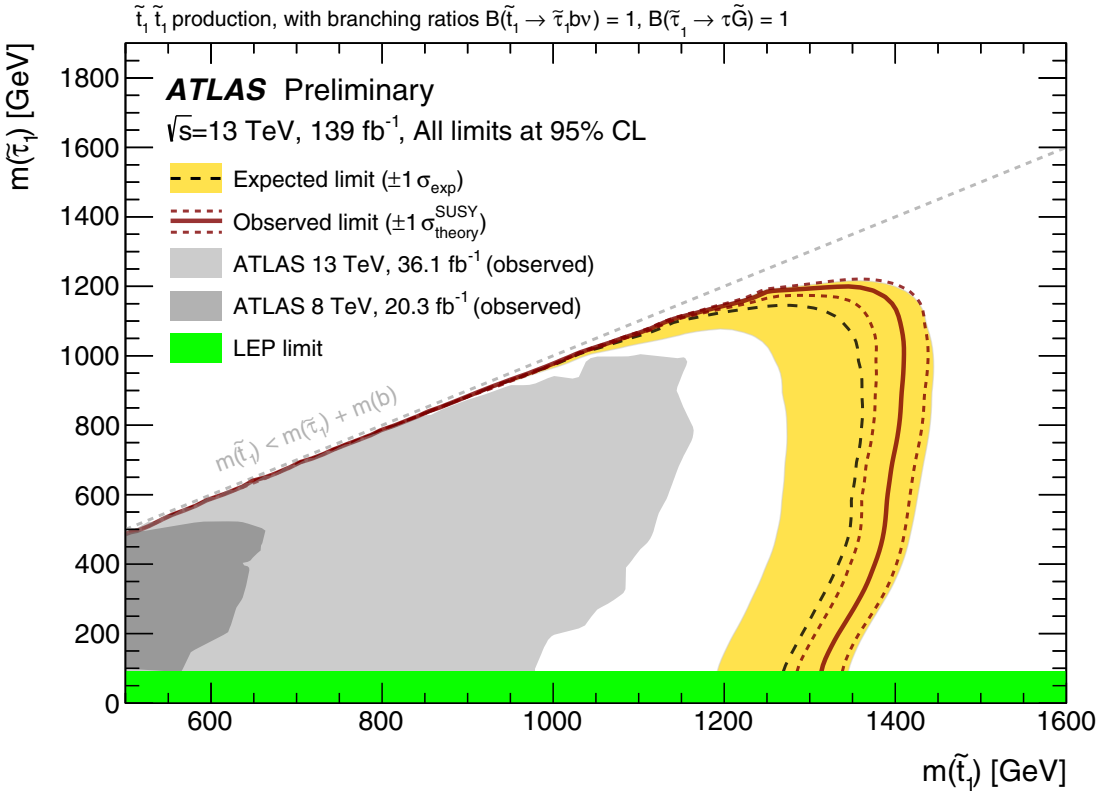

Figure 8: Exclusion contours at the 95 % confidence level for the stop-stau signal model as a function of the masses of the top squark $m(\tilde{t})$ and of the tau slepton $m(\tilde{\tau})$. Expected and observed limits are shown for the present search in comparison to observed limits from previous ATLAS analyses based on data from Run-1 of the LHC at $\sqrt{s} = 8$ TeV [50] and on a partial dataset from Run-2 at $\sqrt{s} = 13$ TeV [51]. The green band indicates the limit on the mass of the tau slepton (for a massless LSP) from the LEP experiments [134].

In the absence of a significant excess, the analysis results are interpreted in terms of exclusion limits on the parameters of the stop-stau and leptoquark signal models. The limits are derived from a model-dependent exclusion fit, which includes the signal regions in addition to the control regions, and signal contributions are taken into account in all analysis regions. The signal contamination of the control regions does not exceed 10 (12) % for model parameters that have not been excluded by previous searches for the stop-stau (leptoquark) signal. Whether the signal-plus-background hypothesis is compatible with the observed event yields is evaluated using the CL_s prescription [135], for which the p-values are computed with asymptotic formulae obtained for a profile-likelihood ratio as the test statistic [124]. The validity of the asymptotic formulae has been checked through a comparison with the results from pseudo experiments in the case of the model-independent limits. The likelihood is the product of Poisson terms modeling the joint probability of the event yields for all analysis regions considered in the fit and Gaussian probability terms that constrain the nuisance parameters related to the systematic uncertainties. Figure 8 shows the expected and observed exclusion contours at the 95 % confidence level for the stop-stau signal computed from the model-dependent exclusion fit that includes both the di-tau and single-tau multi-bin SR. All systematic uncertainties are included in the fit with the exception of the signal cross-section uncertainty, for which a separate band around the observed limit contour is drawn instead. The expected exclusion reach of the analysis extends to top-squark masses around 1.35 TeV over a wide range of tau-slepton masses, and to tau-slepton masses

around 1.15 TeV. With decreasing tau-slepton mass, most noticeably below 400 GeV, the exclusion reach in top-squark mass becomes slightly lower, because the fraction of $E_{\mathrm{T}}^{\mathrm{miss}}$ that is due to the neutrinos from the top-squark decay increases, and thus the discrimination power of m_{T2} is reduced. The observed exclusion slightly exceeds the expected exclusion reach, as the sensitivity to the stop-stau model for tau-slepton masses larger than 200 GeV is dominated by the di-tau SR with an observed deficit. Top-squark masses of up to 1.4 TeV and tau-slepton masses of up to 1.2 TeV are excluded at the 95 % confidence level in this specific model. These are the strongest mass limits for these two supersymmetric particles in a simplified model from Run-2 of the LHC to date. They extend significantly beyond the limits from the previous ATLAS analysis, which are shown in the plot for comparison. The gain in sensitivity is partly due to the larger dataset used in the analysis, but also due to improved reconstruction and identification algorithms for tau leptons and b-jets, and an improved signal-region strategy with reoptimized selection requirements and the added single-tau signal region targeting low tau-slepton masses.

Exclusion limits for the leptoquark signal are shown in the two plots in Fig. 9, where the upper plot considers pair production of up-type leptoquarks $\mathrm{LQ}_3^{\mathrm{u}}$ and the bottom plot pair production of down-type leptoquarks $\mathrm{LQ}_3^{\mathrm{d}}$. To derive these exclusion limits, the fit includes, besides the four CRs, only the single-tau multi-bin SR. The di-tau SR has not been optimized for the leptoquark models, as final states with two tau leptons are covered by a previous search [56], and this SR does therefore not contribute to the exclusion sensitivity. For both types of leptoquarks, the expected and observed exclusion contours extend to masses around 1.25 TeV at the 95 % confidence level for intermediate values of the branching fraction $B(\mathrm{LQ}_3^{\mathrm{u/d}} \to q\ell)$. When $B(\mathrm{LQ}_3^{\mathrm{u/d}} \to q\ell)$ approaches zero or one, the fraction of events with exactly one tau lepton decreases accordingly, leading to a reduction of the signal acceptance and thus a lower mass reach.

In addition to the model-dependent interpretations for the two signal models shown above, model-independent statements about the presence of physics that is not included in the background expectation for SM processes can be derived from the analysis results as well. The model-independent fit is performed for each of the one-bin SRs of the two analysis channels separately. As no specific model is assumed, the contamination of the CRs by a potential signal is neglected, and a generic signal of variable strength is included in the SR. Table 7 states the observed S_{obs}^{95} and expected upper limits S_{exp}^{95} on the number of signal events at the 95 % confidence level based on the CL_s prescription, where the test statistic is evaluated using pseudo experiments. These upper limits are also expressed as upper limits on the visible signal cross section $\langle A\epsilon\sigma\rangle_{\mathrm{obs}}^{95}$, which is defined as the product of acceptance A, reconstruction efficiency ϵ and signal cross section σ. The table also reports the CL_b value, i. e. the confidence level observed for the background-only hypothesis, the discovery p-value $p(s = 0)$, which quantifies the probability to observe at least as many events as expected under the background-only hypothesis, and the associated significance for each of the two channels.

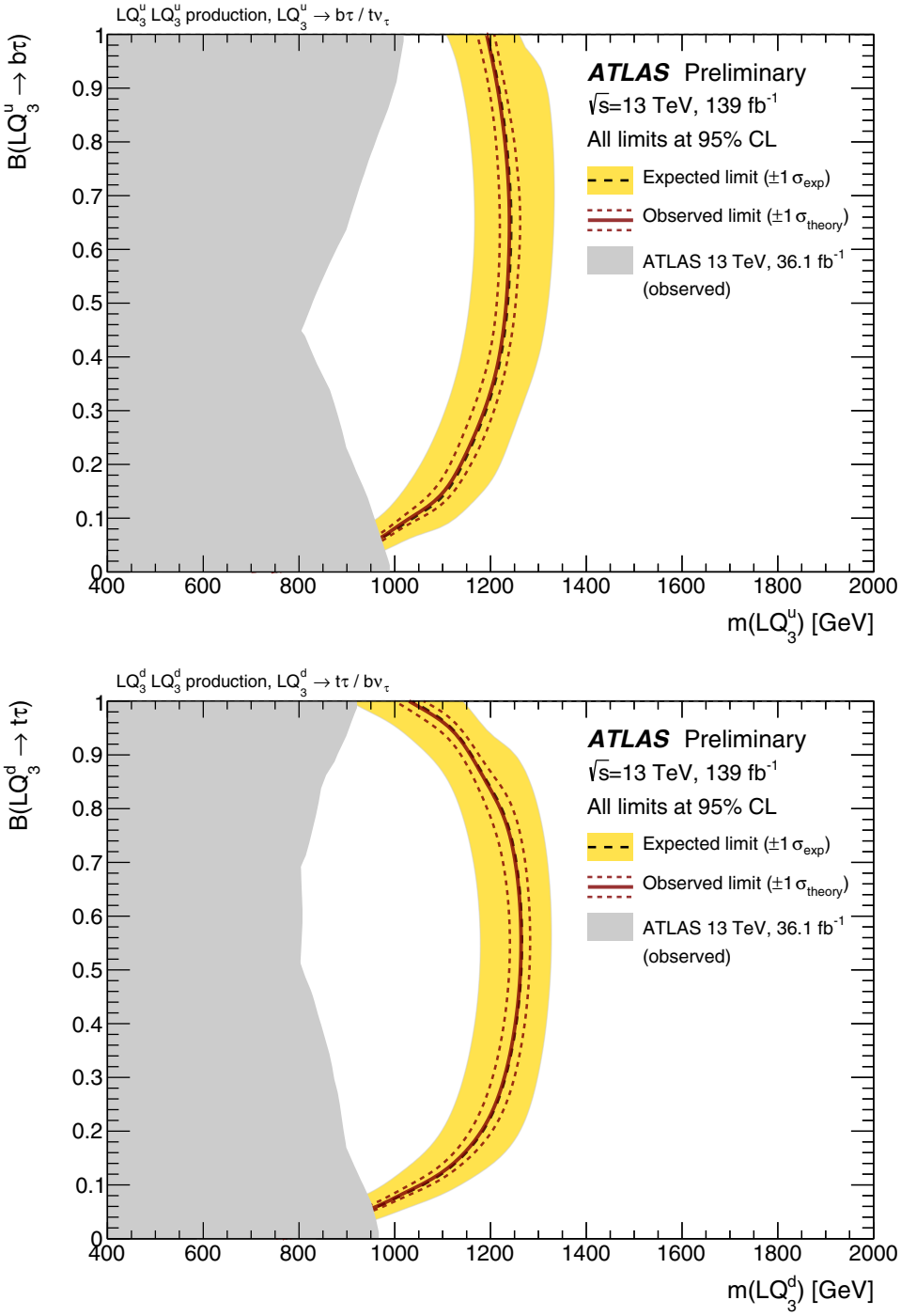

Figure 9: Expected and observed exclusion contours at the 95 % confidence level for the leptoquarks signal model, as a function of $m(\mathrm{LQ}_3)$ and the branching fraction $B(\mathrm{LQ}_3^{u/d} \to q\ell)$ into charged leptons. The top plot shows the exclusion contour for scalar third-generation leptoquarks LQ_3^u with charge $+2/3e$, the bottom plot the exclusion contour for scalar third-generation leptoquarks LQ_3^d with charge $-1/3e$. The limits are derived from the binned single-tau signal region. Shown in gray for comparison are the observed exclusion-limit contours from the previous ATLAS publication that targets the same leptoquark models but is based on a subset of the Run-2 data [54]. In this previous publication five different analyses are considered that target not only the final state studied here but also the final states that correspond to a branching fraction $B(\mathrm{LQ}_3^{u/d} \to q\ell)$ of 0 or 1 into a charged lepton and a quark, leading to the concave shapes of the gray exclusion contours.

Table 7: Left to right: upper limits at the 95 % confidence level (CL) on the visible cross section ($\langle A\epsilon\sigma\rangle^{95}_{\text{obs}}$) and on the number of signal events (S^{95}_{obs}). The third column (S^{95}_{exp}) shows the upper limit at the 95 % CL on the number of signal events, given the expected number (and $\pm 1\,\sigma$ excursions on the expectation) of background events. The last two columns indicate the CL_b value, i. e. the confidence level observed for the background-only hypothesis, the discovery p-value $p(s = 0)$ and the significance Z. In the di-tau SR, where fewer events are observed than predicted by the fitted background estimate, the p-value is capped at 0.5.

Signal channel	$\langle A\epsilon\sigma\rangle^{95}_{\text{obs}}$ [fb]	S^{95}_{obs}	S^{95}_{exp}	CL_b	$p(s = 0)$ (Z)
Di-tau SR	0.03	4.1	$5.3^{+2.2}_{-1.5}$	0.18	0.50 (0.0)
Single-tau one-bin SR	0.06	8.2	$5.1^{+2.1}_{-1.3}$	0.91	0.08 (1.37)

9 Conclusion

In this note, a search for new phenomena in final states with hadronically decaying tau leptons, b-jets and large missing transverse momentum is presented. This signature provides sensitivity to models in which the new particles preferentially decay into third-generation Standard Model particles. The analysis exploits the full dataset recorded with the ATLAS detector in Run 2 of the LHC, corresponding to 139 fb^{-1} of proton–proton collisions at $\sqrt{s} = 13$ TeV. No significant excess of events is observed over the Standard Model expectation. The results are thus interpreted in terms of exclusion limits at 95 % confidence level for two simplified models with pair production of supersymmetric top squarks or scalar leptoquarks which are assumed to only decay into third-generation fermions. In the case of the supersymmetric model, masses up to 1.4 TeV are excluded for top squarks decaying via tau sleptons into nearly massless gravitinos across a wide range of tau-slepton masses. For both up-type and down-type leptoquarks, masses of up to around 1.25 TeV can be excluded. The larger dataset, updated reconstruction and identifications algorithms for tau leptons and b-jets, and the optimized analysis strategy yield a significantly improved sensitivity compared to earlier LHC studies. Based on the two considered benchmark models, the interpretation of the results presents the strongest mass limits to date on pair-produced top squarks and on pair-produced third-generation scalar leptoquarks with similar branching fractions into charged and uncharged leptons.

References

[1] Y. Golfand and E. Likhtman, *Extension of the Algebra of Poincare Group Generators and Violation of P Invariance*, JETP Lett. **13** (1971) 323, [Pisma Zh. Eksp. Teor. Fiz. **13** (1971) 452] (cit. on p. 2).

[2] D. Volkov and V. Akulov, *Is the neutrino a goldstone particle?* Phys. Lett. B **46** (1973) 109 (cit. on p. 2).

[3] J. Wess and B. Zumino, *Supergauge transformations in four dimensions*, Nucl. Phys. B **70** (1974) 39 (cit. on p. 2).

[4] J. Wess and B. Zumino, *Supergauge invariant extension of quantum electrodynamics*, Nucl. Phys. B **78** (1974) 1 (cit. on p. 2).

[5] S. Ferrara and B. Zumino, *Supergauge invariant Yang-Mills theories*, Nucl. Phys. B **79** (1974) 413 (cit. on p. 2).

[6] A. Salam and J. Strathdee, *Super-symmetry and non-Abelian gauges*, Phys. Lett. B **51** (1974) 353 (cit. on p. 2).

[7] S. P. Martin, *A Supersymmetry Primer*, Adv. Ser. Direct. High Energy Phys. **18** (1998) 1, arXiv: hep-ph/9709356 (cit. on p. 2).

[8] N. Sakai, *Naturalness in supersymmetric GUTS*, Z. Phys. C **11** (1981) 153 (cit. on p. 2).

[9] S. Dimopoulos, S. Raby, and F. Wilczek, *Supersymmetry and the scale of unification*, Phys. Rev. D **24** (1981) 1681 (cit. on p. 2).

[10] L. E. Ibáñez and G. G. Ross, *Low-energy predictions in supersymmetric grand unified theories*, Phys. Lett. B **105** (1981) 439 (cit. on p. 2).

[11] S. Dimopoulos and H. Georgi, *Softly broken supersymmetry and SU(5)*, Nucl. Phys. B **193** (1981) 150 (cit. on p. 2).

[12] G. R. Farrar and P. Fayet, *Phenomenology of the production, decay, and detection of new hadronic states associated with supersymmetry*, Phys. Lett. B **76** (1978) 575 (cit. on p. 2).

[13] H. Goldberg, *Constraint on the Photino Mass from Cosmology*, Phys. Rev. Lett. **50** (1983) 1419 (cit. on p. 2), Erratum: Phys. Rev. Lett. **103** (2009) 099905.

[14] J. Ellis, J. Hagelin, D. V. Nanopoulos, K. A. Olive, and M. Srednicki, *Supersymmetric relics from the big bang*, Nucl. Phys. B **238** (1984) 453 (cit. on p. 2).

[15] W. De Boer, *Grand unified theories and supersymmetry in particle physics and cosmology*, Progress in Particle and Nuclear Physics **33** (1994) 201, ISSN: 0146-6410, arXiv: 9402266 [hep-ph] (cit. on p. 2).

[16] H. Georgi and S. Glashow, *Unity of All Elementary Particle Forces*, Phys. Rev. Lett. **32** (1974) 438 (cit. on p. 2).

[17] S. K. Dimopoulos and L. Susskind, *Mass without scalars*, Nucl. Phys. B **155** (1979) 237 (cit. on p. 2).

[18] S. Dimopoulos, *Technicoloured signatures*, Nucl. Phys. B **168** (1980) 69 (cit. on p. 2).

[19] E. J. Eichten and K. Lane, *Dynamical breaking of weak interaction symmetries*, Phys. Lett. B **90** (1980) 125 (cit. on p. 2).

[20] V. D. Angelopoulos, J. R. Ellis, H. Kowalski, et al., *Search for new quarks suggested by the superstring*, Nucl. Phys. B **292** (1987) 59 (cit. on p. 2).

[21] W. Buchmüller and D. Wyler, *Constraints on SU(5)-type leptoquarks*, Phys. Lett. B **177** (1986) 377 (cit. on p. 2).

[22] G. Hiller and M. Schmaltz, *R_K and future $b \to s\ell\ell$ physics beyond the standard model opportunities*, Phys. Rev. D **90** (2014) 054014, arXiv: 1408.1627 [hep-ph] (cit. on p. 2).

[23] B. Gripaios, M. Nardecchia, and S. A. Renner, *Composite leptoquarks and anomalies in B-meson decays*, JHEP **05** (2015) 006, arXiv: 1412.1791 [hep-ph] (cit. on p. 2).

[24] M. Freytsis, Z. Ligeti, and J. T. Ruderman, *Flavor models for $\bar{B} \to D^{(*)}\tau\bar{\nu}$*, Phys. Rev. D **92** (2015) 054018, arXiv: 1506.08896 [hep-ph] (cit. on p. 2).

[25] M. Bauer and M. Neubert, *Minimal Leptoquark Explanation for the $R_{D^{(*)}}$, R_K , and $(g-2)_g$ Anomalies*, Phys. Rev. Lett. **116** (2016) 141802, arXiv: 1511.01900 [hep-ph] (cit. on p. 2).

[26] L. Di Luzio and M. Nardecchia, *What is the scale of new physics behind the B-flavour anomalies?* Eur. Phys. J. C **77** (2017) 536, arXiv: 1706.01868 [hep-ph] (cit. on p. 2).

[27] D. Buttazzo, A. Greljo, G. Isidori, and D. Marzocca, *B-physics anomalies: a guide to combined explanations*, JHEP **11** (2017) 044, arXiv: 1706.07808 [hep-ph] (cit. on p. 2).

[28] J. M. Cline, *B decay anomalies and dark matter from vectorlike confinement*, Phys. Rev. D **97** (2018) 015013, arXiv: 1710.02140 [hep-ph] (cit. on p. 2).

[29] BaBar Collaboration, *Measurement of an excess of $\bar{B} \to D^{(*)}\tau^-\bar{\nu}_\tau$ decays and implications for charged Higgs bosons*, Phys. Rev. D **88** (2013) 072012, arXiv: 1303.0571 (cit. on p. 2).

[30] Belle Collaboration, *Measurement of the branching ratio of $\bar{B} \to D^{(*)}\tau^-\bar{\nu}_\tau$ relative to $\bar{B} \to D^{(*)}\ell^-\bar{\nu}_\ell$ decays with hadronic tagging at Belle*, Phys. Rev. D **92** (2015) 072014, arXiv: 1507.03233 (cit. on p. 2).

[31] LHCb Collaboration, *Measurement of the Ratio of Branching Fractions $\mathcal{B}(\bar{B}^0 \to D^{*+}\tau^-\bar{\nu}_\tau)/\mathcal{B}(\bar{B}^0 \to D^{*+}\mu^-\bar{\nu}_\mu)$*, Phys. Rev. Lett. **115** (2015) 111803, arXiv: 1506.08614, Erratum: Phys. Rev. Lett. **115** (2015) 159901 (cit. on p. 2).

[32] Belle Collaboration, *Measurement of the τ lepton polarization and $R(D^*)$ in the decay $\bar{B} \to D^*\tau^-\bar{\nu}_\tau$*, Phys. Rev. Lett. **118** (2017) 211801, arXiv: 1612.00529 [hep-ex] (cit. on p. 2).

[33] LHCb Collaboration, *Measurement of the ratio of branching fractions $\mathcal{B}(B_c^+ \to J/\psi\tau^+\nu_\tau)/\mathcal{B}(B_c^+ \to J/\psi\mu^+\nu_\mu)$*, Phys. Rev. Lett. **120** (2018) 121801, arXiv: 1711.05623 [hep-ex] (cit. on p. 2).

[34] LHCb Collaboration, *Angular analysis of the $B^0 \to K^{*0}\mu^+\mu^-$ decay using 3 fb^{-1} of integrated luminosity*, JHEP **02** (2016) 104, arXiv: 1512.04442 [hep-ex] (cit. on p. 2).

[35] Belle Collaboration, *Lepton-Flavor-Dependent Angular Analysis of $B \to K^*\ell^+\ell^-$*, Phys. Rev. Lett. **118** (2017) 111801, arXiv: 1612.05014 [hep-ex] (cit. on p. 2).

[36] LHCb Collaboration, *Test of lepton universality with $B^0 \to K^{*0}\ell^+\ell^-$ decays*, JHEP **08** (2017) 055, arXiv: 1705.05802 (cit. on p. 2).

[37] LHCb Collaboration, *Search for Lepton-Universality Violation in $B^+ \to K^+\ell^+\ell^-$ Decays*, Phys. Rev. Lett. **122** (2019) 191801, arXiv: 1903.09252 (cit. on p. 2).

[38] M. Dine and W. Fischler, *A phenomenological model of particle physics based on supersymmetry*, Phys. Lett. B **110** (1982) 227 (cit. on p. 2).

[39] L. Alvarez-Gaume, M. Claudson, and M. B. Wise, *Low-energy supersymmetry*, Nucl. Phys. B **207** (1982) 96 (cit. on p. 2).

[40] C. R. Nappi and B. A. Ovrut, *Supersymmetric extension of the SU(3) x SU(2) x U(1) model*, Phys. Lett. B **113** (1982) 175 (cit. on p. 2).

[41] M. Asano, H. D. Kim, R. Kitano, and Y. Shimizu, *Natural supersymmetry at the LHC*, JHEP **2010** (2010) 19, ISSN: 1029-8479, URL: https://doi.org/10.1007/JHEP12(2010)019 (cit. on p. 2).

[42] K. Inoue, A. Kakuto, H. Komatsu, and S. Takeshita, *Aspects of Grand Unified Models with Softly Broken Supersymmetry*, Prog. Theor. Phys. **68** (1982) 927 (cit. on p. 2), Erratum: Prog. Theor. Phys. **70** (1983) 330.

[43] J. R. Ellis and S. Rudaz, *Search for supersymmetry in toponium decays*, Phys. Lett. B **128** (1983) 248 (cit. on p. 2).

[44] J. Alwall, M.-P. Le, M. Lisanti, and J. G. Wacker, *Searching for directly decaying gluinos at the Tevatron*, Phys. Lett. B **666** (2008) 34, arXiv: 0803.0019 [hep-ph] (cit. on p. 2).

[45] J. Alwall, P. Schuster, and N. Toro, *Simplified models for a first characterization of new physics at the LHC*, Phys. Rev. D **79** (2009) 075020, arXiv: 0810.3921 [hep-ph] (cit. on p. 2).

[46] D. Alves et al., *Simplified models for LHC new physics searches*, J. Phys. G **39** (2012) 105005, arXiv: 1105.2838 [hep-ph] (cit. on p. 2).

[47] ATLAS Collaboration, *Search for a scalar partner of the top quark in the all-hadronic $t\bar{t}$ plus missing transverse momentum final state at $\sqrt{s}$ = 13 TeV with the ATLAS detector*, Eur. Phys. J. C **80** (2020) 737, arXiv: 2004.14060 [hep-ex] (cit. on pp. 2, 4).

[48] ATLAS Collaboration, *Search for new phenomena with top quark pairs in final states with one lepton, jets, and missing transverse momentum in pp collisions at $\sqrt{s}$= 13 TeV with the ATLAS detector*, (2020), submitted to JHEP, arXiv: 2012.03799 [hep-ex] (cit. on p. 2).

[49] ATLAS Collaboration, *Search for new phenomena in events with two opposite-charge leptons, jets and missing transverse momentum in pp collisions at $\sqrt{s}$ = 13 TeV with the ATLAS detector*, ATLAS-CONF-2020-046, 2020, URL: https://cds.cern.ch/record/2728056 (cit. on p. 2).

[50] ATLAS Collaboration, *Search for direct top squark pair production in final states with two tau leptons in pp collisions at $\sqrt{s}$ = 8 TeV with the ATLAS detector*, Eur. Phys. J. C **76** (2016) 81, arXiv: 1509.04976 [hep-ex] (cit. on pp. 3, 20).

[51] ATLAS Collaboration, *Search for top squarks decaying to tau sleptons in pp collisions at $\sqrt{s}$ = 13 TeV with the ATLAS detector*, Phys. Rev. D **98** (2018) 032008, arXiv: 1803.10178 [hep-ex] (cit. on pp. 3, 4, 20).

[52] CMS Collaboration, *Search for top squark pair production in a final state with two tau leptons in proton–proton collisions at $\sqrt{s}$ = 13 TeV*, JHEP **02** (2020) 015, arXiv: 1910.12932 [hep-ex] (cit. on p. 3).

[53] W. Buchmüller, R. Rückl, and D. Wyler, *Leptoquarks in lepton - quark collisions*, Phys. Lett. B **191** (1987) 442 (cit. on pp. 3, 6), Erratum: Phys. Lett. B **448** (1999) 320.

[54] ATLAS Collaboration, *Searches for third-generation scalar leptoquarks in $\sqrt{s}$ = 13 TeV pp collisions with the ATLAS detector*, JHEP **06** (2019) 144, arXiv: 1902.08103 [hep-ex] (cit. on pp. 4, 22).

[55] ATLAS Collaboration, *Search for new phenomena in final states with b-jets and missing transverse momentum in $\sqrt{s}$ = 13 TeV pp collisions with the ATLAS detector*, (2021), submitted to JHEP, arXiv: 2101.12527 [hep-ex] (cit. on p. 4).

[56] ATLAS Collaboration, *Search for pair production of third-generation scalar leptoquarks decaying into a top quark and a τ-lepton in pp collisions at $\sqrt{s}$ = 13 TeV with the ATLAS detector*, (2021), submitted to JHEP, arXiv: 2101.11582 [hep-ex] (cit. on pp. 4, 21).

[57] CMS Collaboration, *Search for singly and pair-produced leptoquarks coupling to third-generation fermions in proton-proton collisions at $\sqrt{s}$ = 13 TeV*, (2020), submitted to PLB, arXiv: 2012.04178 [hep-ex] (cit. on p. 4).

[58] CMS Collaboration, *Constraints on models of scalar and vector leptoquarks decaying to a quark and a neutrino at $\sqrt{s}$ = 13 TeV*, Phys. Rev. D **98** (2018) 032005, arXiv: 1805.10228 [hep-ex] (cit. on p. 4).

[59] CMS Collaboration, *Search for third-generation scalar leptoquarks decaying to a top quark and a τ lepton at $\sqrt{s}$ = 13 TeV*, Eur. Phys. J. C **78** (2018) 707, arXiv: 1803.02864 [hep-ex] (cit. on p. 4).

[60] CMS Collaboration, *Search for Leptoquarks Coupled to Third-Generation Quarks in Proton–Proton Collisions at* $\sqrt{s} = 13$ *TeV*, Phys. Rev. Lett. **121** (2018) 241802, arXiv: 1809.05558 [hep-ex] (cit. on p. 4).

[61] CMS Collaboration, *Search for heavy neutrinos and third-generation leptoquarks in hadronic states of two* τ *leptons and two jets in proton–proton collisions at* $\sqrt{s} = 13$ *TeV*, JHEP **03** (2019) 170, arXiv: 1811.00806 [hep-ex] (cit. on p. 4).

[62] CMS Collaboration, *Search for a singly produced third-generation scalar leptoquark decaying to a* τ *lepton and a bottom quark in proton–proton collisions at* $\sqrt{s} = 13$ *TeV*, JHEP **07** (2018) 115, arXiv: 1806.03472 [hep-ex] (cit. on p. 4).

[63] ATLAS Collaboration, *The ATLAS Experiment at the CERN Large Hadron Collider*, JINST **3** (2008) S08003 (cit. on p. 4).

[64] ATLAS Collaboration, *ATLAS Insertable B-Layer: Technical Design Report*, ATLAS-TDR-19; CERN-LHCC-2010-013, 2010, URL: https://cds.cern.ch/record/1291633 (cit. on p. 4).

[65] B. Abbott et al., *Production and integration of the ATLAS Insertable B-Layer*, JINST **13** (2018) T05008, arXiv: 1803.00844 [physics.ins-det] (cit. on p. 4).

[66] ATLAS Collaboration, *Luminosity determination in pp collisions at* $\sqrt{s} = 13$ *TeV using the ATLAS detector at the LHC*, ATLAS-CONF-2019-021, 2019, URL: https://cds.cern.ch/record/2677054 (cit. on p. 5).

[67] G. Avoni et al., *The new LUCID-2 detector for luminosity measurement and monitoring in ATLAS*, JINST **13** (2018) P07017 (cit. on p. 5).

[68] S. Agostinelli et al., *GEANT4 – a simulation toolkit*, Nucl. Instrum. Meth. A **506** (2003) 250 (cit. on p. 5).

[69] ATLAS Collaboration, *The simulation principle and performance of the ATLAS fast calorimeter simulation FastCaloSim*, ATL-PHYS-PUB-2010-013, 2010, URL: https://cds.cern.ch/record/1300517 (cit. on p. 5).

[70] E. Bothmann et al., *Event generation with Sherpa 2.2*, SciPost Phys. **7** (2019) 034, arXiv: 1905.09127 [hep-ph] (cit. on p. 5).

[71] ATLAS Collaboration, *ATLAS Pythia 8 tunes to 7 TeV data*, ATL-PHYS-PUB-2014-021, 2014, URL: https://cds.cern.ch/record/1966419 (cit. on pp. 5, 16).

[72] D. J. Lange, *The EvtGen particle decay simulation package*, Nucl. Instrum. Meth. A **462** (2001) 152 (cit. on p. 5).

[73] T. Sjöstrand, S. Mrenna, and P. Skands, *A brief introduction to PYTHIA 8.1*, Comput. Phys. Commun. **178** (2008) 852, arXiv: 0710.3820 [hep-ph] (cit. on p. 5).

[74] R. D. Ball et al., *Parton distributions with LHC data*, Nucl. Phys. B **867** (2013) 244, arXiv: 1207.1303 [hep-ph] (cit. on pp. 5, 6).

[75] ATLAS Collaboration, *The Pythia 8 A3 tune description of ATLAS minimum bias and inelastic measurements incorporating the Donnachie–Landshoff diffractive model*, ATL-PHYS-PUB-2016-017, 2016, URL: https://cds.cern.ch/record/2206965 (cit. on p. 5).

[76] S. Frixione, P. Nason, and G. Ridolfi, *A positive-weight next-to-leading-order Monte Carlo for heavy flavour hadroproduction*, JHEP **09** (2007) 126, arXiv: 0707.3088 [hep-ph] (cit. on pp. 5, 6).

[77] P. Nason, *A new method for combining NLO QCD with shower Monte Carlo algorithms*, JHEP **11** (2004) 040, arXiv: hep-ph/0409146 (cit. on pp. 5, 6).

[78] S. Frixione, P. Nason, and C. Oleari, *Matching NLO QCD computations with parton shower simulations: the POWHEG method*, JHEP **11** (2007) 070, arXiv: 0709.2092 [hep-ph] (cit. on pp. 5, 6).

[79] S. Alioli, P. Nason, C. Oleari, and E. Re, *A general framework for implementing NLO calculations in shower Monte Carlo programs: the POWHEG BOX*, JHEP **06** (2010) 043, arXiv: 1002.2581 [hep-ph] (cit. on pp. 5, 6).

[80] T. Sjöstrand et al., *An introduction to PYTHIA 8.2*, Comput. Phys. Commun. **191** (2015) 159, arXiv: 1410.3012 [hep-ph] (cit. on pp. 5, 6).

[81] M. Czakon and A. Mitov, *Top++: A program for the calculation of the top-pair cross-section at hadron colliders*, Comput. Phys. Commun. **185** (2014) 2930, arXiv: 1112.5675 [hep-ph] (cit. on p. 5).

[82] R. D. Ball et al., *Parton distributions for the LHC run II*, JHEP **04** (2015) 040, arXiv: 1410.8849 [hep-ph] (cit. on pp. 5, 6).

[83] E. Re, *Single-top Wt-channel production matched with parton showers using the POWHEG method*, Eur. Phys. J. C **71** (2011) 1547, arXiv: 1009.2450 [hep-ph] (cit. on p. 5).

[84] M. Aliev et al., *HATHOR – HAdronic Top and Heavy quarks crOss section calculatoR*, Comput. Phys. Commun. **182** (2011) 1034, arXiv: 1007.1327 [hep-ph] (cit. on p. 5).

[85] P. Kant et al., *HatHor for single top-quark production: Updated predictions and uncertainty estimates for single top-quark production in hadronic collisions*, Comput. Phys. Commun. **191** (2015) 74, arXiv: 1406.4403 [hep-ph] (cit. on p. 5).

[86] N. Kidonakis, *Two-loop soft anomalous dimensions for single top quark associated production with a W^- or H^-*, Phys. Rev. D **82** (2010) 054018, arXiv: 1005.4451 [hep-ph] (cit. on p. 5).

[87] N. Kidonakis, "Top Quark Production," *Proceedings, Helmholtz International Summer School on Physics of Heavy Quarks and Hadrons (HQ 2013)* (JINR, Dubna, Russia, July 15–28, 2013) 139, arXiv: 1311.0283 [hep-ph] (cit. on p. 5).

[88] C. Anastasiou, L. J. Dixon, K. Melnikov, and F. Petriello, *High precision QCD at hadron colliders: Electroweak gauge boson rapidity distributions at next-to-next-to leading order*, Phys. Rev. D **69** (2004) 094008, arXiv: hep-ph/0312266 (cit. on p. 5).

[89] T. Gleisberg and S. Höche, *Comix, a new matrix element generator*, JHEP **12** (2008) 039, arXiv: 0808.3674 [hep-ph] (cit. on p. 5).

[90] S. Schumann and F. Krauss, *A parton shower algorithm based on Catani–Seymour dipole factorisation*, JHEP **03** (2008) 038, arXiv: 0709.1027 [hep-ph] (cit. on p. 5).

[91] ATLAS Collaboration, *Multi-Boson Simulation for* 13 *TeV ATLAS Analyses*, ATL-PHYS-PUB-2017-005, 2017, URL: https://cds.cern.ch/record/2261933 (cit. on p. 5).

[92] J. Alwall et al., *The automated computation of tree-level and next-to-leading order differential cross sections, and their matching to parton shower simulations*, JHEP **07** (2014) 079, arXiv: 1405.0301 [hep-ph] (cit. on pp. 5, 6).

[93] ATLAS Collaboration, *Modelling of the $t\bar{t}H$ and $t\bar{t}V(V = W, Z)$ processes for $\sqrt{s} = 13$ TeV ATLAS analyses*, ATL-PHYS-PUB-2016-005, 2016, URL: https://cds.cern.ch/record/2120826 (cit. on p. 5).

[94] H. B. Hartanto, B. Jäger, L. Reina, and D. Wackeroth, *Higgs boson production in association with top quarks in the POWHEG BOX*, Phys. Rev. D **91** (2015) 094003, arXiv: 1501.04498 [hep-ph] (cit. on p. 5).

[95] W. Beenakker, C. Borschensky, M. Krämer, A. Kulesza, and E. Laenen, *NNLL-fast: predictions for coloured supersymmetric particle production at the LHC with threshold and Coulomb resummation*, JHEP **12** (2016) 133, arXiv: 1607.07741 [hep-ph] (cit. on pp. 5, 6).

[96] W. Beenakker, M. Krämer, T. Plehn, M. Spira, and P. Zerwas, *Stop production at hadron colliders*, Nucl. Phys. B **515** (1998) 3, arXiv: hep-ph/9710451 (cit. on pp. 5, 6).

[97] W. Beenakker et al., *Supersymmetric top and bottom squark production at hadron colliders*, JHEP **08** (2010) 098, arXiv: 1006.4771 [hep-ph] (cit. on pp. 5, 6).

[98] W. Beenakker et al., *NNLL resummation for stop pair-production at the LHC*, JHEP **05** (2016) 153, arXiv: 1601.02954 [hep-ph] (cit. on pp. 5, 6).

[99] P. Artoisenet, R. Frederix, O. Mattelaer, and R. Rietkerk, *Automatic spin-entangled decays of heavy resonances in Monte Carlo simulations*, JHEP **03** (2013) 015, arXiv: 1212.3460 [hep-ph] (cit. on p. 6).

[100] L. Lönnblad, *Correcting the Colour-Dipole Cascade Model with Fixed Order Matrix Elements*, JHEP **05** (2002) 046, arXiv: hep-ph/0112284 (cit. on p. 6).

[101] L. Lönnblad and S. Prestel, *Matching tree-level matrix elements with interleaved showers*, JHEP **03** (2012) 019, arXiv: 1109.4829 [hep-ph] (cit. on p. 6).

[102] T. Mandal, S. Mitra, and S. Seth, *Pair production of scalar leptoquarks at the LHC to NLO parton shower accuracy*, Phys. Rev. D **93** (2016) 035018, arXiv: 1506.07369 [hep-ph] (cit. on p. 6).

[103] M. Kramer, T. Plehn, M. Spira, and P. Zerwas, *Pair production of scalar leptoquarks at the CERN LHC*, Phys. Rev. D **71** (2005) 057503, arXiv: hep-ph/0411038 (cit. on p. 6).

[104] M. Kramer, T. Plehn, M. Spira, and P. Zerwas, *Pair Production of Scalar Leptoquarks at the Tevatron*, Phys. Rev. Lett. **79** (1997) 341, arXiv: hep-ph/9704322 (cit. on p. 6).

[105] A. Belyaev, C. Leroy, R. Mehdiyev, and A. Pukhov, *Leptoquark single and pair production at LHC with CalcHEP/CompHEP in the complete model*, JHEP **09** (2005) 005, arXiv: hep-ph/0502067 [hep-ph] (cit. on p. 6).

[106] C. Borschensky, B. Fuks, A. Kulesza, and D. Schwartländer, *Scalar leptoquark pair production at hadron colliders*, Phys. Rev. D **101** (2020) 115017, arXiv: 2002.08971 [hep-ph] (cit. on p. 6).

[107] ATLAS Collaboration, *Vertex Reconstruction Performance of the ATLAS Detector at* $\sqrt{s} = 13$ *TeV*, ATL-PHYS-PUB-2015-026, 2015, URL: https://cds.cern.ch/record/2037717 (cit. on p. 6).

[108] ATLAS Collaboration, *Jet reconstruction and performance using particle flow with the ATLAS Detector*, Eur. Phys. J. C **77** (2017) 466, arXiv: 1703.10485 [hep-ex] (cit. on p. 6).

[109] ATLAS Collaboration, *Jet energy scale measurements and their systematic uncertainties in proton–proton collisions at* $\sqrt{s} = 13$ *TeV with the ATLAS detector*, Phys. Rev. D **96** (2017) 072002, arXiv: 1703.09665 [hep-ex] (cit. on p. 6).

[110] ATLAS Collaboration, *Selection of jets produced in* 13 *TeV proton–proton collisions with the ATLAS detector*, ATLAS-CONF-2015-029, 2015, URL: https://cds.cern.ch/record/2037702 (cit. on p. 6).

[111] ATLAS Collaboration, *Tagging and suppression of pileup jets with the ATLAS detector*, ATLAS-CONF-2014-018, 2014, URL: https://cds.cern.ch/record/1700870 (cit. on p. 7).

[112] ATLAS Collaboration, *ATLAS b-jet identification performance and efficiency measurement with $t\bar{t}$ events in pp collisions at $\sqrt{s}$ = 13 TeV*, Eur. Phys. J. C **79** (2019) 970, arXiv: 1907.05120 [hep-ex] (cit. on p. 7).

[113] ATLAS Collaboration, *Optimisation and performance studies of the ATLAS b-tagging algorithms for the 2017-18 LHC run*, ATL-PHYS-PUB-2017-013, 2017, URL: https://cds.cern.ch/record/2273281 (cit. on p. 7).

[114] ATLAS Collaboration, *Readiness of the ATLAS liquid argon calorimeter for LHC collisions*, Eur. Phys. J. C **70** (2010) 723, arXiv: 0912.2642 [hep-ex] (cit. on p. 7).

[115] ATLAS Collaboration, *Identification and energy calibration of hadronically decaying tau leptons with the ATLAS experiment in pp collisions at $\sqrt{s}$ = 8 TeV*, Eur. Phys. J. C **75** (2015) 303, arXiv: 1412.7086 [hep-ex] (cit. on p. 7).

[116] ATLAS Collaboration, *Measurement of the tau lepton reconstruction and identification performance in the ATLAS experiment using pp collisions at $\sqrt{s}$ = 13 TeV*, ATLAS-CONF-2017-029, 2017, URL: https://cds.cern.ch/record/2261772 (cit. on p. 7).

[117] ATLAS Collaboration, *Reconstruction of hadronic decay products of tau leptons with the ATLAS experiment*, Eur. Phys. J. C **76** (2016) 295, arXiv: 1512.05955 [hep-ex] (cit. on p. 7).

[118] ATLAS Collaboration, *Identification of hadronic tau lepton decays using neural networks in the ATLAS experiment*, ATL-PHYS-PUB-2019-033, 2019, URL: https://cds.cern.ch/record/2688062 (cit. on p. 7).

[119] ATLAS Collaboration, *Electron reconstruction and identification in the ATLAS experiment using the 2015 and 2016 LHC proton–proton collision data at $\sqrt{s}$ = 13 TeV*, Eur. Phys. J. C **79** (2019) 639, arXiv: 1902.04655 [hep-ex] (cit. on p. 7).

[120] ATLAS Collaboration, *Electron and photon performance measurements with the ATLAS detector using the 2015–2017 LHC proton–proton collision data*, JINST **14** (2019) P12006, arXiv: 1908.00005 [hep-ex] (cit. on pp. 7, 8).

[121] ATLAS Collaboration, *Muon reconstruction performance of the ATLAS detector in proton–proton collision data at $\sqrt{s}$ = 13 TeV*, Eur. Phys. J. C **76** (2016) 292, arXiv: 1603.05598 [hep-ex] (cit. on p. 7).

[122] ATLAS Collaboration, *Performance of missing transverse momentum reconstruction with the ATLAS detector using proton–proton collisions at $\sqrt{s}$ = 13 TeV*, Eur. Phys. J. C **78** (2018) 903, arXiv: 1802.08168 [hep-ex] (cit. on p. 8).

[123] ATLAS Collaboration, *E_T^{miss} performance in the ATLAS detector using 2015–2016 LHC pp collisions*, ATLAS-CONF-2018-023, 2018, URL: https://cds.cern.ch/record/2625233 (cit. on p. 8).

[124] G. Cowan, K. Cranmer, E. Gross, and O. Vitells, *Asymptotic formulae for likelihood-based tests of new physics*, Eur. Phys. J. C **71** (2011) 1554, arXiv: 1007.1727 [physics.data-an] (cit. on pp. 8, 18, 20), Erratum: Eur. Phys. J. C **73** (2013) 2501.

[125] C. G. Lester and D. J. Summers, *Measuring masses of semi-invisibly decaying particles pair produced at hadron colliders*, Phys. Lett. B **463** (1999) 99, arXiv: hep-ph/9906349 [hep-ph] (cit. on p. 9).

[126] C. G. Lester and B. Nachman, *Bisection-based asymmetric M_{T2} computation: a higher precision calculator than existing symmetric methods*, JHEP **03** (2015) 100, arXiv: 1411.4312 [hep-ph] (cit. on p. 9).

[127] M. Baak et al., *HistFitter software framework for statistical data analysis*, Eur. Phys. J. C **75** (2015) 153, arXiv: 1410.1280 [hep-ex] (cit. on p. 10).

[128] J. Butterworth et al., *PDF4LHC recommendations for LHC Run II*, J. Phys. G **43** (2016) 023001, arXiv: 1510.03865 [hep-ph] (cit. on p. 16).

[129] S. Frixione, E. Laenen, P. Motylinski, C. White, and B. R. Webber, *Single-top hadroproduction in association with a W boson*, JHEP **07** (2008) 029, arXiv: 0805.3067 [hep-ph] (cit. on pp. 16, 18).

[130] S. Catani, F. Krauss, R. Kuhn, and B. R. Webber, *QCD Matrix Elements + Parton Showers*, JHEP **11** (2001) 063, arXiv: hep-ph/0109231 (cit. on p. 16).

[131] S. Höche, F. Krauss, S. Schumann, and F. Siegert, *QCD matrix elements and truncated showers*, JHEP **05** (2009) 053, arXiv: 0903.1219 [hep-ph] (cit. on p. 16).

[132] ATLAS Collaboration, *Probing the Quantum Interference between Singly and Doubly Resonant Top-Quark Production in pp Collisions at $\sqrt{s} = 13$ TeV with the ATLAS Detector*, Phys. Rev. Lett. **121** (2018) 152002, arXiv: 1806.04667 [hep-ex] (cit. on p. 18).

[133] ATLAS Collaboration, *Studies on top-quark Monte Carlo modelling for Top2016*, ATL-PHYS-PUB-2016-020, 2016, URL: https://cds.cern.ch/record/2216168 (cit. on p. 18).

[134] The LEP2 SUSY Working Group and ALEPH, DELPHI, L3, OPAL Experiments, *Combined LEP Selectron/Smuon/Stau Results, 183-208 GeV*, http://lepsusy.web.cern.ch/lepsusy/www/sleptons_summer04/slep_final.html, 2004 (cit. on p. 20).

[135] A. L. Read, *Presentation of search results: the CL_S technique*, J. Phys. G **28** (2002) 2693 (cit. on p. 20).